Supporting Information

Photocatalytic Hydrogen Generation from a Visible-Light Responsive Metal-Organic Framework System: The Impact of Nickel Phosphide Nanoparticles

Stavroula Kampouri,[a] Tu N. Nguyen,[a] Christopher P. Ireland,[a] Bardiya Valizadeh,[a] Fatmah Mish Ebrahim,[a] Gloria Capano,[a] Daniele Ongari,[a] Amber Mace,[ab] Nestor Guijarro Carratala,[c] Kevin Sivula,[c] Andrzej Sienkiewicz,[d] László Forró,[d] Berend Smit,[a] Kyriakos C. Stylianou[a]*

Table of Contents

S1. General Methods

Materials: 2-aminobenzene-1,4-dicarboxylic acid (NH_2-H_2BDC, 99%), titanium isopropoxide ($Ti(OCH(CH_3)_2)_4$, 97%), nickel nitrate hexahydrate ($Ni(NO_3)_2{\cdot}6H_2O$, 99.999% trace metal basis), anhydrous N,N-dimethylformamide (DMF; $(CH_3)_2NCHO$, 99.8%), anhydrous methanol (CH_3OH, 99.8%), acetonitrile (CH_3CN, ≥ 99.5), sodium hypophosphite (NaH_2PO_2, ≥ 99%), triethylamine (TEA, ≥ 99%) and P25 Titanium(IV) oxide (TiO_2, nanopowder, ~21 nm, ≥ 99.5%) were purchased from Sigma Aldrich. Benzene-1,3,5-tricarboxylic acid ($C_6H_3(COOH)_3$, H_3BTC, > 98.0%) was purchased from TCI. All the materials were used as received without further purification.

Powder X-ray Diffraction (PXRD) data were collected on a Bruker D8 Advance diffractometer at ambient temperature using monochromated Cu Kα radiation (λ= 1.5418 Å), with a 2θ step size of 0.02° and a 2θ range of ~2 to 70°. The Fourier-transform infrared (FTIR) measurements were carried out with the Spectrum Two FTIR spectrometer (PerkinElmer). The Nitrogen adsorption-desorption isotherms were collected using a BEL-SORP mini (BEL Japan, Inc.) at 77 K. Prior to data collection, the samples were degassed at 423 K for 12 h. The BET surface areas were estimated from the amount of N_2 adsorption at 77 K using the BET (Brunauer-Emmett-Teller) equilibrium equation. The morphology, size and elemental analysis of Ni_2P NPs, Ni_2P/MIL-125-NH_2 and MIL-125-NH_2 were investigated by using high resolution transmission electron microscopy (TEM) on FEI Tecnai Osiris instrument and scanning electron microscopy (SEM) on FEI Teneo instrument, equipped with an energy dispersive X-ray (EDX) detector (XFlash Silicon drift detector). The UV-Vis absorbance and diffuse reflectance spectra were obtained with a PerkinElmer UV-Vis Spectrometer. Photoluminescence (PL) spectra (excitation at 360 and 420 nm) were measured with a Fluorescence Spectrometer LS 55 (PerkinElmer). The time-resolved PL was carried out using an Edinburgh transient absorption spectrometer (LP980), with the excitation wavelength of 420 nm. Inductively coupled plasma optical emission spectrometry (ICP-OES) measurements were performed using a NexIon 350 (Perkin Elmer) spectrometer. Low-temperature electron paramagnetic resonance (LT-EPR) measurements were carried out using a Bruker EleXsys E500 X-band (9.4 GHz) EPR spectrometer (Bruker BioSpin GmbH, Karlsruhe, Germany), which was equipped with a high-Q cylindrical cavity, Model ER 4122 SHQE, and a helium gas-flow cryostat, ESR900 (Oxford Instruments Ltd., Tubney Woods, Abington, England). At cryogenic temperatures, the sample temperature was stabilized and monitored by an ITC503 temperature controller (Oxford Instruments Ltd.). In this study, all EPR spectra were acquired at 20 K.

S2. Synthesis of MIL-125-NH_2

The MOF was synthesized by following a reported procedure.[1] 0.286 g of NH_2-H_2BDC was dissolved in a mixture of 4.0 mL of anhydrous DMF and 1.0 mL of anhydrous methanol. 0.286 ml of titanium isopropoxide was added in the mixture, which was sonicated for 30 min and then heated up to 120 °C for 72h. The obtained product with a yield of ~75-80%, was washed several times with DMF and methanol. Consequently it was dispersed in DMF and kept under stirring for 12 h, in order to remove residual linker. This procedure was repeated twice using methanol in order to exchange the DMF within the pores. Finally the as-synthesized powder was dried at room temperature.

S3. Synthesis of Ni_2P NPs

Ni_2P NPs were synthesized based on a reported procedure.[2] First, the Ni-BTC MOF was synthesized by dissolving 0.255 g of $Ni(NO_3)_2{\cdot}6H_2O$ and 0.102 g H_3BTC in 14.0 mL of methanol and then heating the mixture up to 150 °C for 24 h in a Teflon liner inserted in a stainless steel autoclave. The obtained solid was washed several times with methanol and then dried under vacuum at 60 °C.

In a typical preparation of Ni_2P nanoparticles, 0.10 g of the as-prepared Ni–BTC and 0.30 g of NaH_2PO_2 were mixed together, loaded into a ceramic crucible, and heated to 275 °C for 2 h in a furnace. After cooling to room temperature, the product was washed with water and ethanol and dried under vacuum at 60 °C for 6 h. The overall yield of the Ni_2P synthesis was estimated at around 25-30%.

S4. Powder X-ray Diffraction

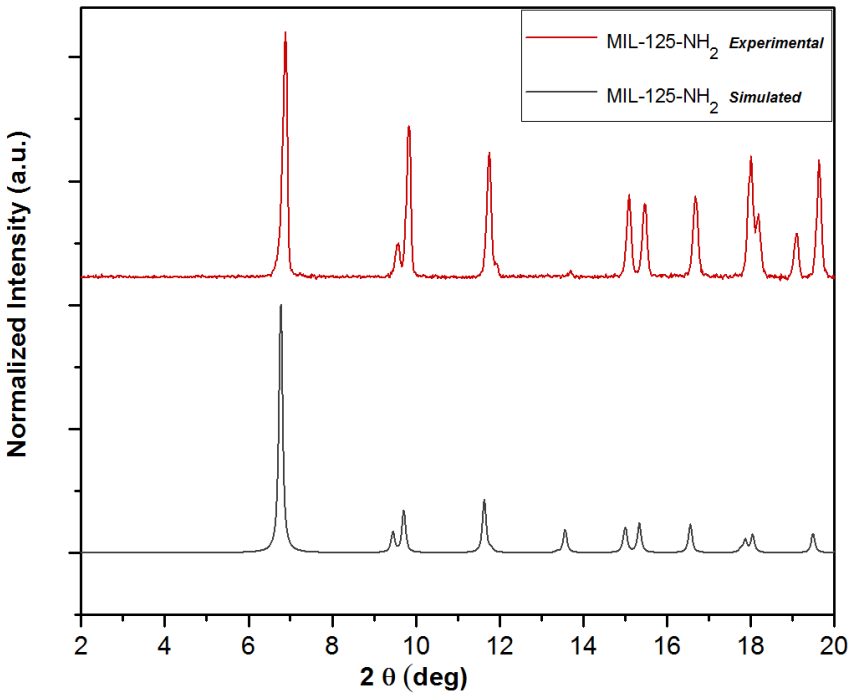

Figure S1. Powder X-ray diffraction patterns of the as synthesized (red) and simulated (grey) MIL-125-NH_2. The simulated PXRD pattern is in agreement with the experimental pattern confirming that MIL-125-NH_2 can be obtained as pure phase.

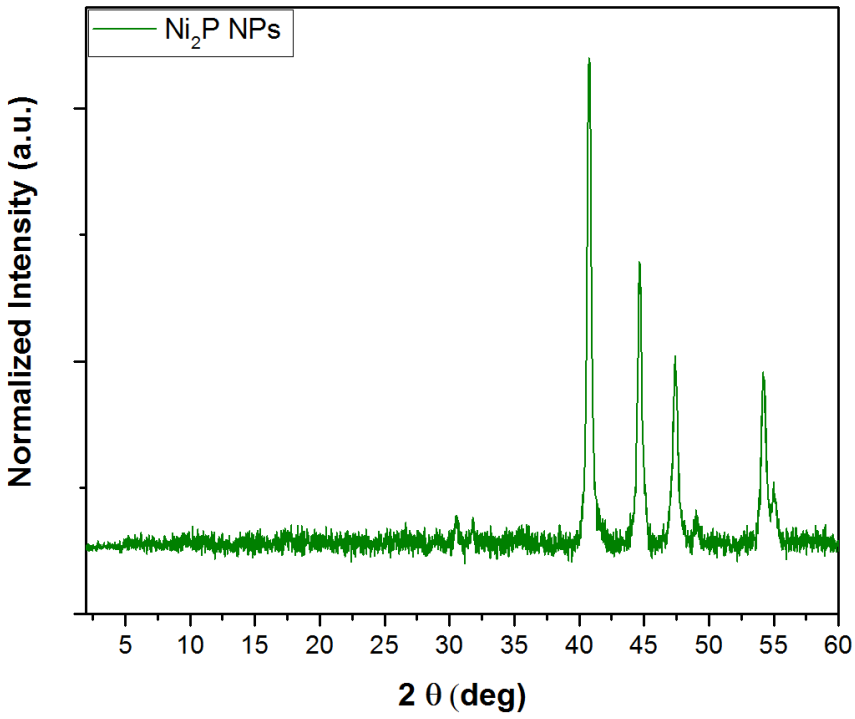

Figure S2. Powder X-ray diffraction pattern of the Ni_2P NPs.

S5. High Resolution TEM, SEM and EDX

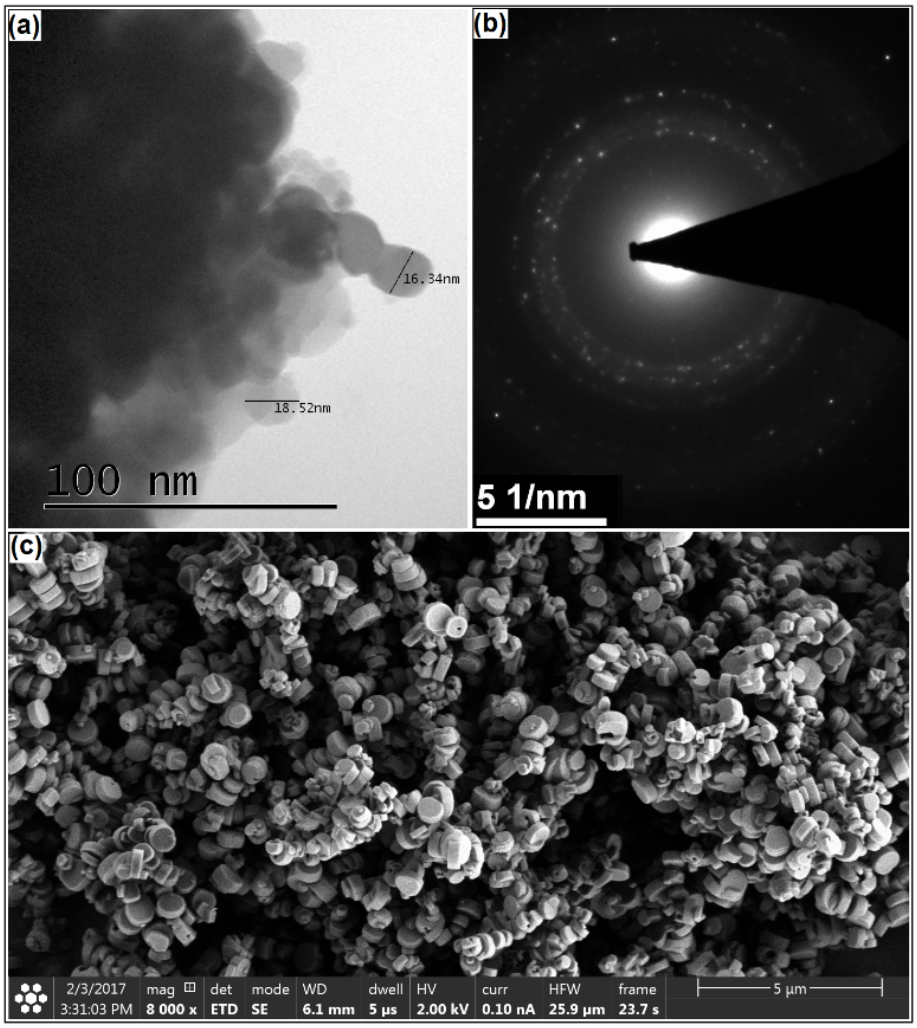

Figure S3. (a) High-Resolution TEM image shows that the size of Ni_2P NPs is between 16-19 nm, and (b) Electron Diffraction pattern of Ni_2P NPs. (c) SEM image of the as synthesized MIL-125-NH_2.

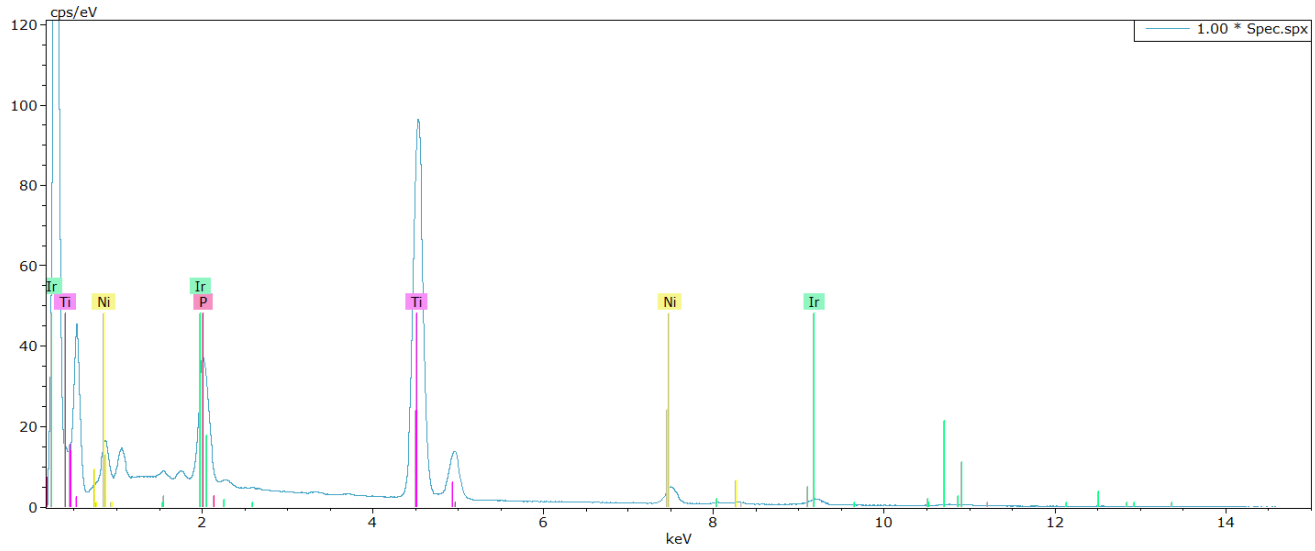

Figure S4. EDX spectrum of the Ni_2P/MIL-125-NH_2.

*note: The sample was coated with Iridium for SEM and EDX analysis.

S6. N_2 Adsorption-Desorption Isotherms

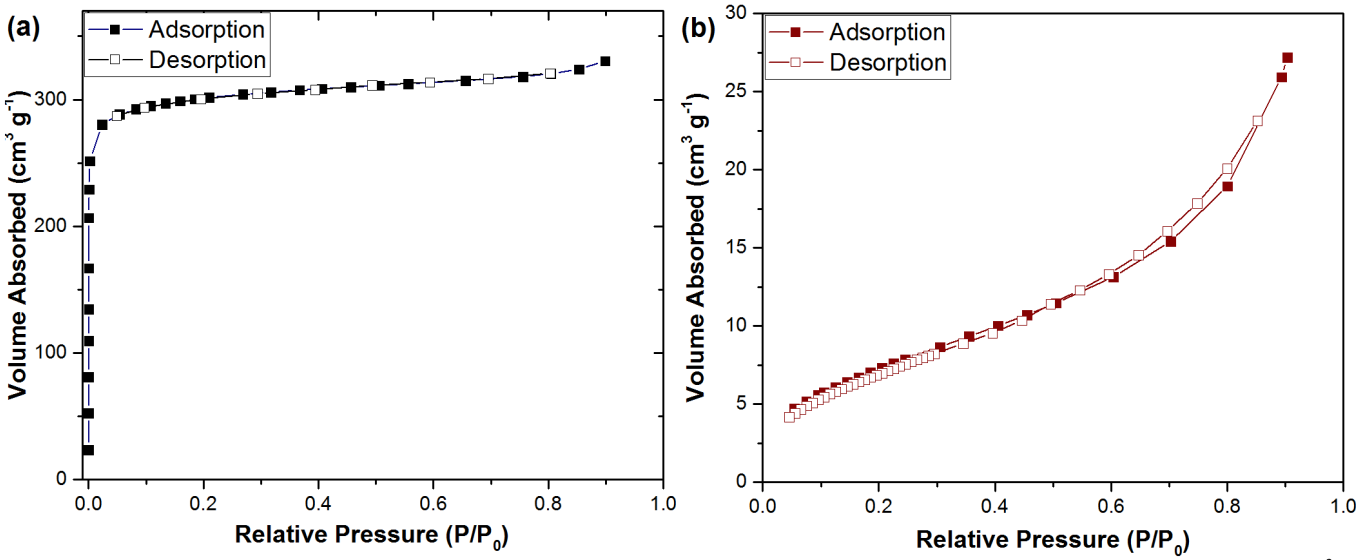

Figure S5. (a) N_2 adsorption-desorption isotherm of MIL-125-NH_2 showing that MIL-125-NH_2 is a microporous material with BET surface area of 1197 m^2 g^{-1}, and (b) N_2 adsorption-desorption isotherm of Ni_2P NPs with BET surface area of 27 m^2 g^{-1}.

S7. UV-Vis Spectroscopy

The diffuse reflectance and absorbance spectra of MIL-125-NH_2 and the free ligand NH_2-H_2BDC (Fig. S6) show that MIL-125-NH_2 displays a red-shift attributed to the ligand-to-metal charge transfer (LMCT) leading to a strong absorption in the 300-480 nm region. The calculated optical gap of MIL-125-NH_2 is ~2.6 eV.

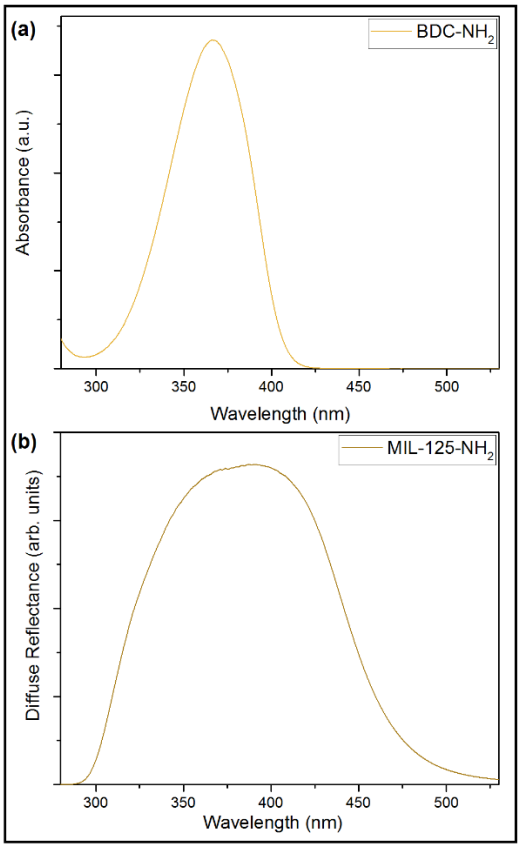

Figure S6. (a) UV-Vis absorbance of H_2BDC-NH_2 in methanol. (b) UV-Vis Diffuse Reflectance of MIL-125-NH_2. The red-shift of light absorption of MIL-125-NH2 is due to LMCT.

S8. Photocatalytic Hydrogen Production

The photocatalytic experiments were performed in a 25 mL Pyrex glass reactor, at room temperature under continuously visible light irradiation from a 300 W Xe lamp equipped with a UV cut-off filter (λ > 420 nm) (Scheme 1). In a typical experiment, 17.0 mg of the catalyst was suspended in 17.0 ml of a photocatalytic solution consisted of acetonitrile, trimethylamine, and deionized water in a volumetric ratio of 5 : 1 : 0.1 respectively. Then, the suspension was purged with nitrogen for 20 min under gentle stirring, in order to remove dissolved oxygen. 200 µL of the gaseous product was abstracted from the head space and analyzed by gas chromatography (PerkinElmer Clarus 480 GC, N_2 carrier gas), equipped with a thermal conductivity detector and a molecular sieve 5 A column.

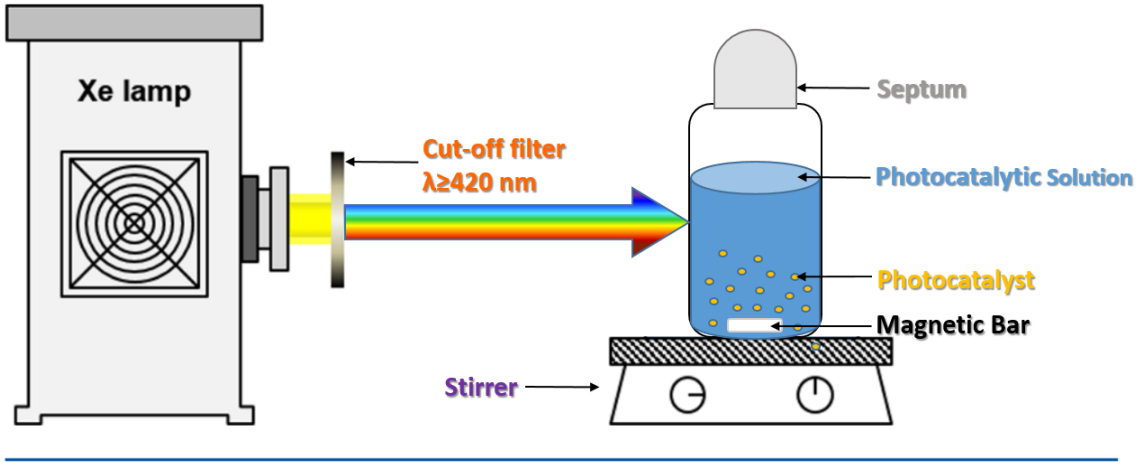

Scheme 1: Schematic illustration of the photocatalytic set up.

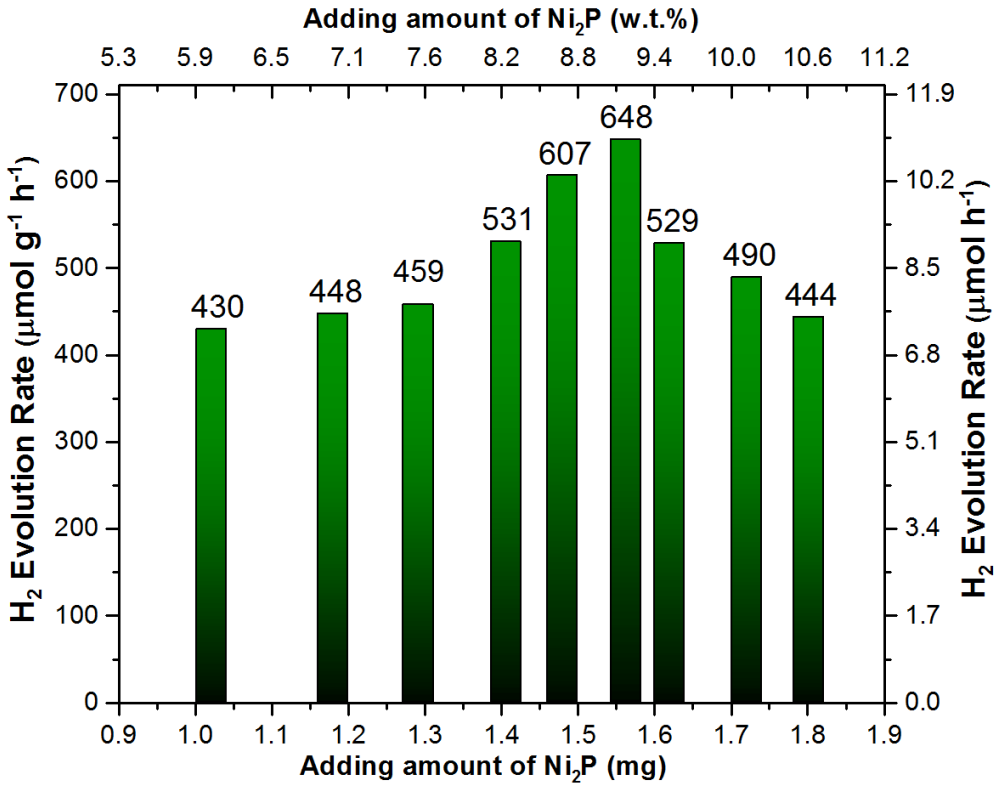

Figure S7. Photocatalytic H_2 evolution rate of 17.0 mg of MIL-125-NH_2 against different adding amounts of Ni_2P NPs – optimisation of the mixing amount of Ni_2P.

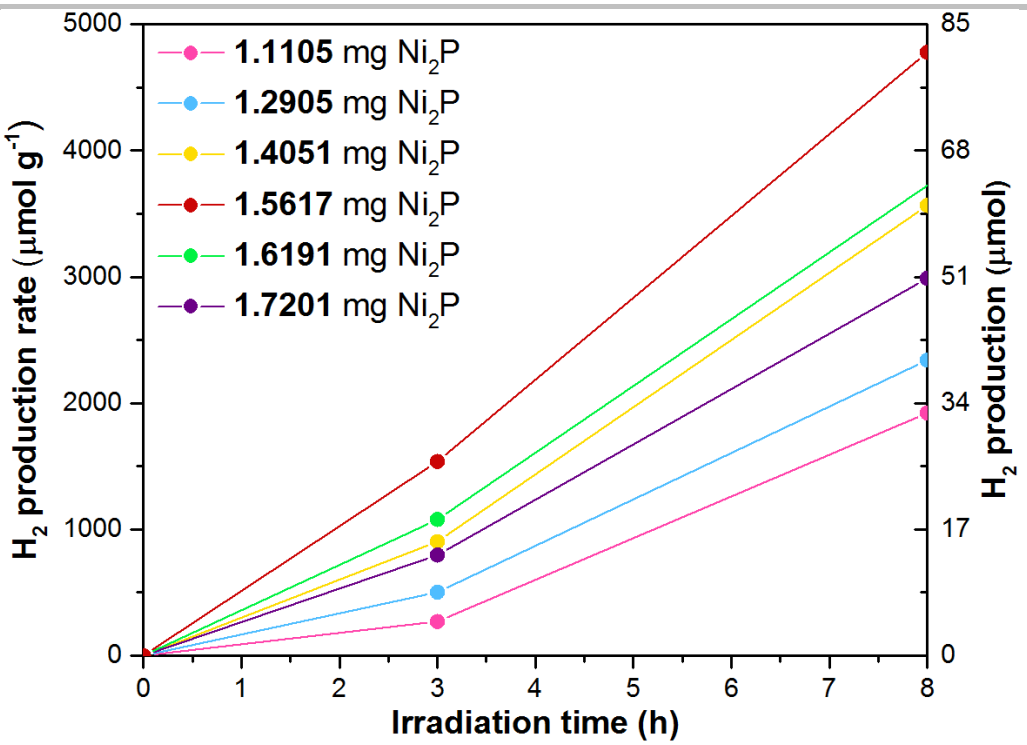

Figure S8. Photocatalytic Hydrogen production of 17.0 mg MIL-125-NH_2 with different adding amounts of Ni_2P NPs.

Control experiments:

In order to confirm the crucial role of MIL-125-NH_2 as a visible-light-active photocatalyst, we performed blank experiments using Ni_2P nanoparticles (NPs) with and without the free ligand NH_2-H_2BDC, suspended in 17 mL of the photocatalytic solution. The amount of Ni_2P NPs used for this purpose was ~1.56 mg, the same amount as that in the optimized 9.2 (±0.4) wt% Ni_2P/MIL-125-NH_2 system. The amount of the free ligand used was 11 mg, which corresponds to the amount of the NH_2-BDC ligand in 17 mg of MIL-125-NH_2, based on the molecular formula ($[Ti_8O_8(OH)_4(O_2C\text{-}C_6H_3NH_2\text{-}CO_2)_6]$).[3] The blank suspensions were irradiated continuously for 24 h under visible light, using the same set up that was used for the visible-light driven photocatalytic experiments for the Ni_2P/MIL-125-NH_2 series .

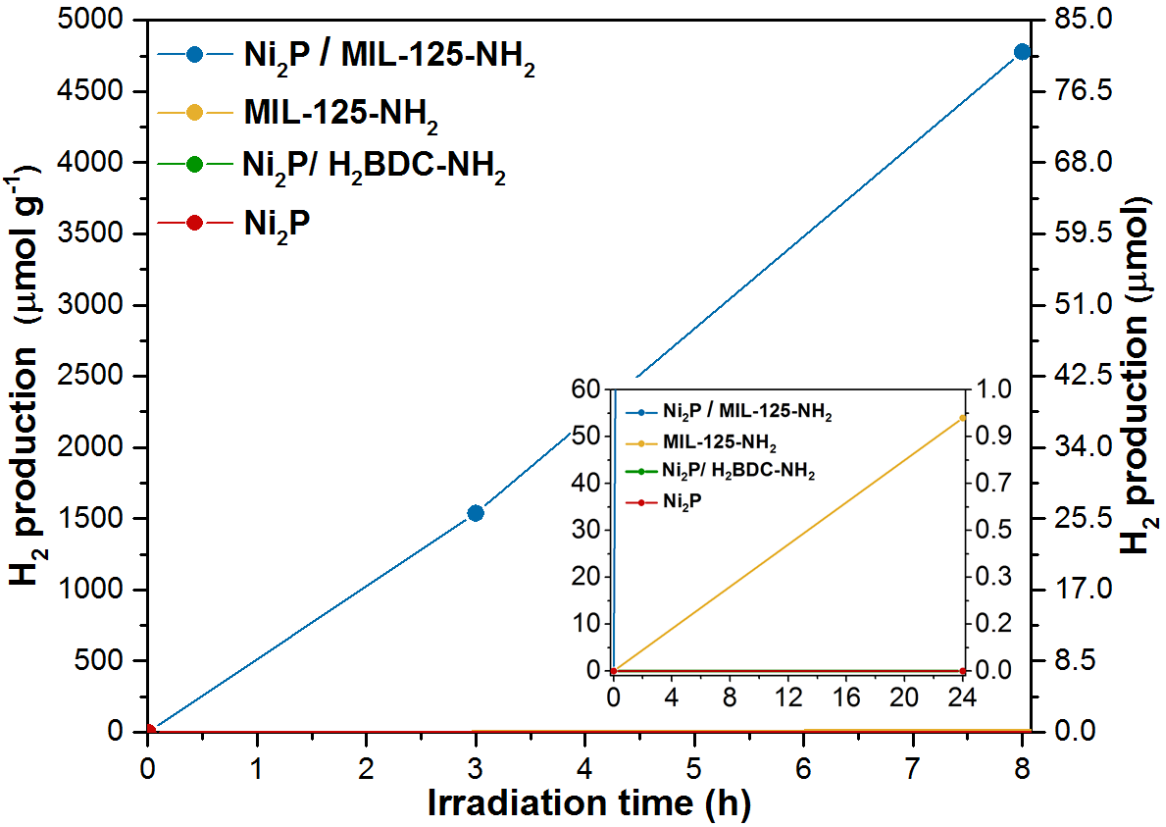

Figure S9. Photocatalytic H_2 production of 9.2 (± 0.4) w.t.% Ni_2P/MIL-125-NH_2 (blue), MIL-125-NH_2 (yellow), Ni_2P/H_2BDC-NH_2 (green) and Ni_2P (red), under visible light irradiation (λ ≥ 420 nm) over 8 hours.

Recycling experiments:

In order to examine the stability of the photocatalytic system, recycling experiments were performed for the optimized 9.2 (± 0.4) wt% Ni_2P/MIL-125-NH_2 system (17 mg of MIL-125-NH_2), which involved seven photocatalytic runs, each for 12 hours. After irradiation and prior to each cycle, the septum was first removed from the Pyrex glass reactor, in order for the suspension to be ventilated, and then the sample was purged with nitrogen for 20 min.

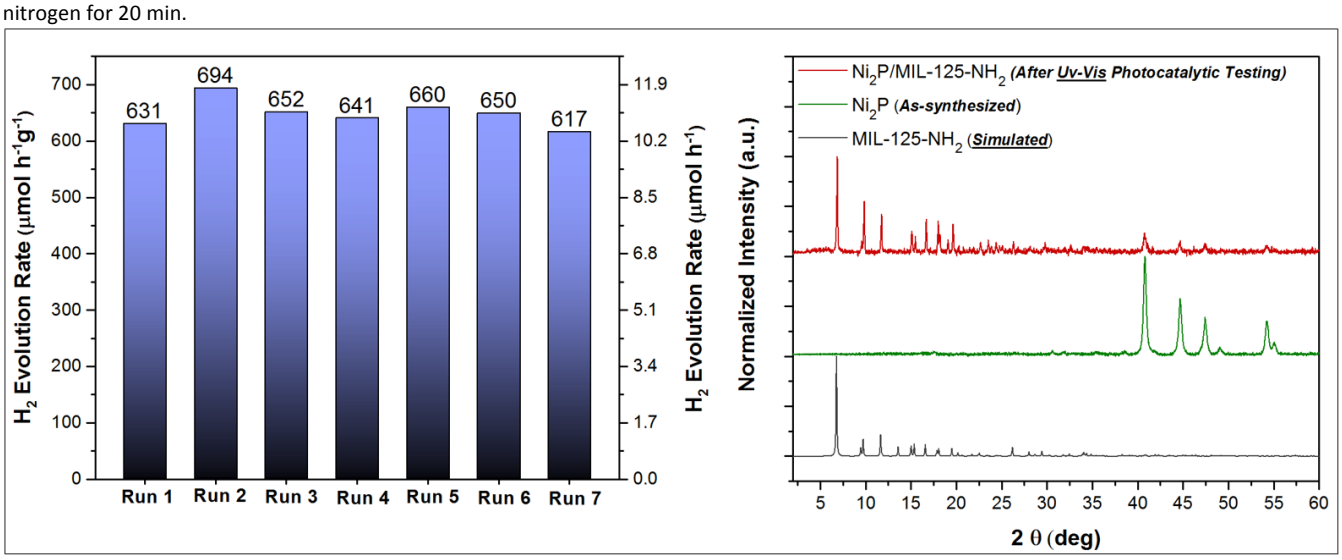

Figure S10. (Left) Recycling performance of 9.2 (± 0.4) wt% Ni_2P/MIL-125-NH_2; and (Right) Powder X-ray diffraction patterns of simulated MIL-125-NH_2 (dark gray), as synthesised Ni_2P NPs (green) and Ni_2P/MIL-125-NH_2 after 84 h of photocatalytic recycling test under visible irradiation (red).

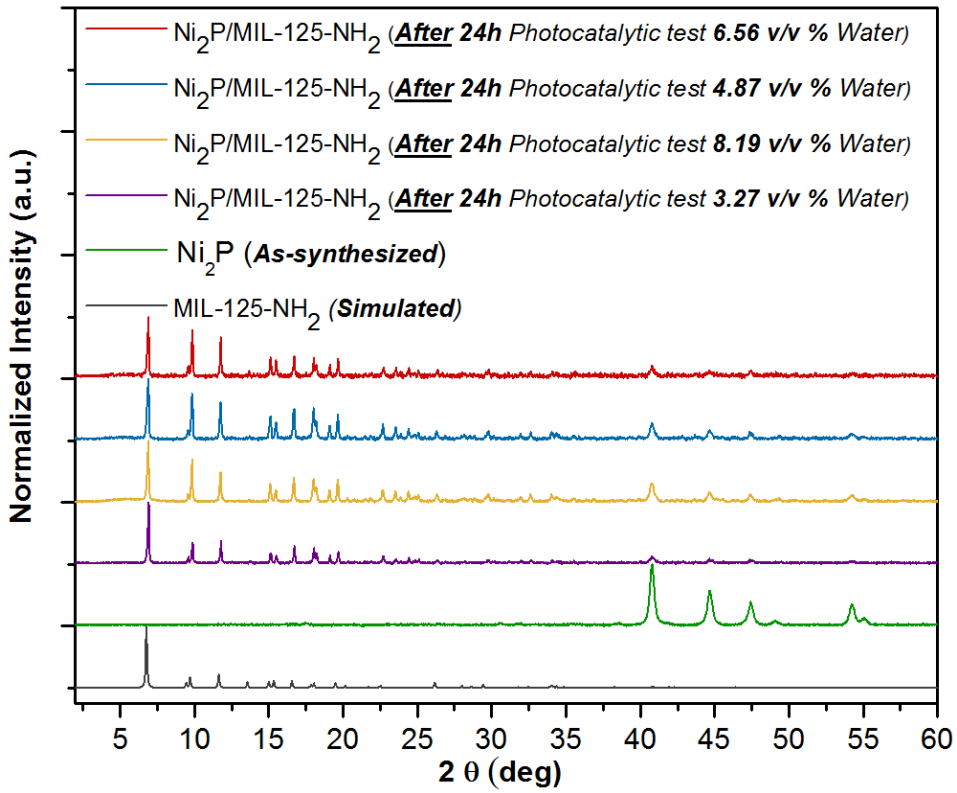

Figure S11. Powder X-ray diffraction patterns of Ni_2P/MIL-125-NH_2 after 24 h of photocatalytic test under visible light irradiation in solutions containing different water contents. The PXRD patterns show that both MIL-125-NH_2 and Ni_2P are stable and retain their structural integrity after photocatalysis.

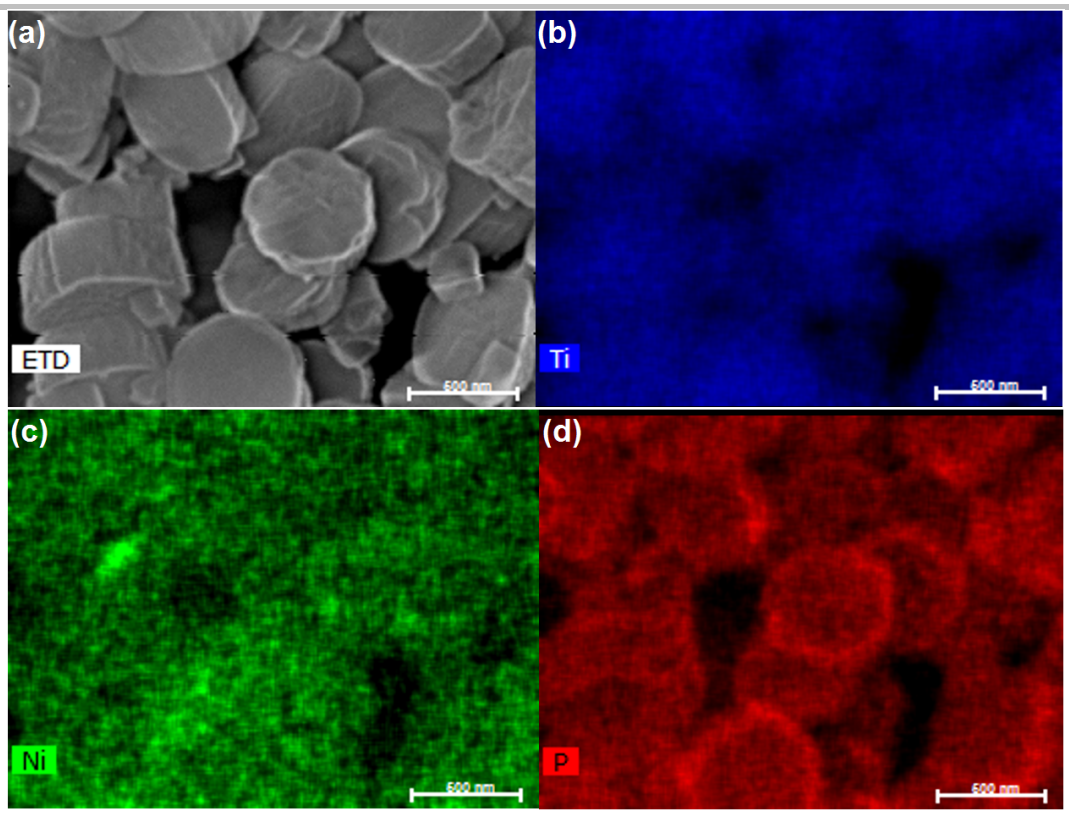

Figure S12. (a) SEM image of 9.2 (± 0.4) wt% Ni_2P/MIL-125-NH_2 (17 mg of MIL-125-NH_2) before photocatalytic testing, and the corresponding EDX maps of (b) Titanium, (c) Nickel and (d) Phosphorus. As can be seen, there is a homogeneous distribution of Ni_2P on MIL-125-NH_2.

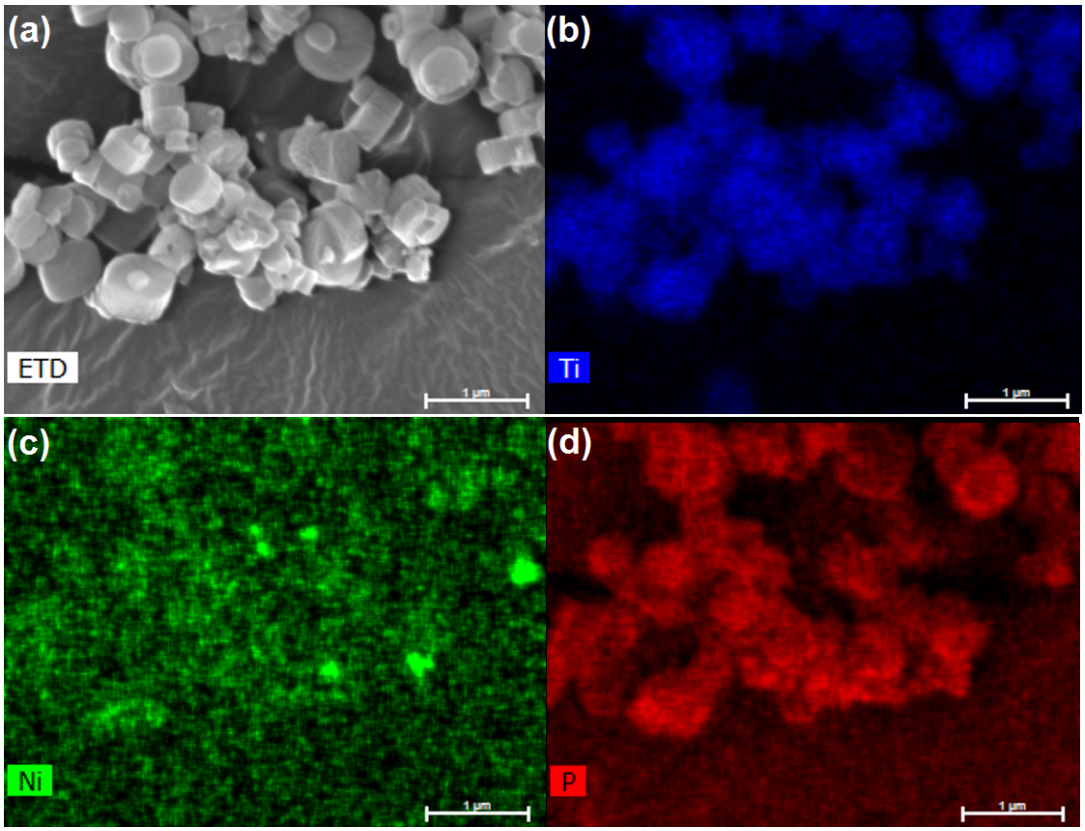

Figure S13. (a) SEM image of 9.2 (± 0.4) wt% Ni_2P/MIL-125-NH_2 (17 mg of MIL-125-NH_2) after recycling experiments, and the corresponding EDX maps of (b) Titanium, (c) Nickel and (d) Phosphorus. As can be seen, there is a homogeneous distribution of Ni_2P on MIL-125-NH_2 and these images are very comparable with those before photocatalysis.

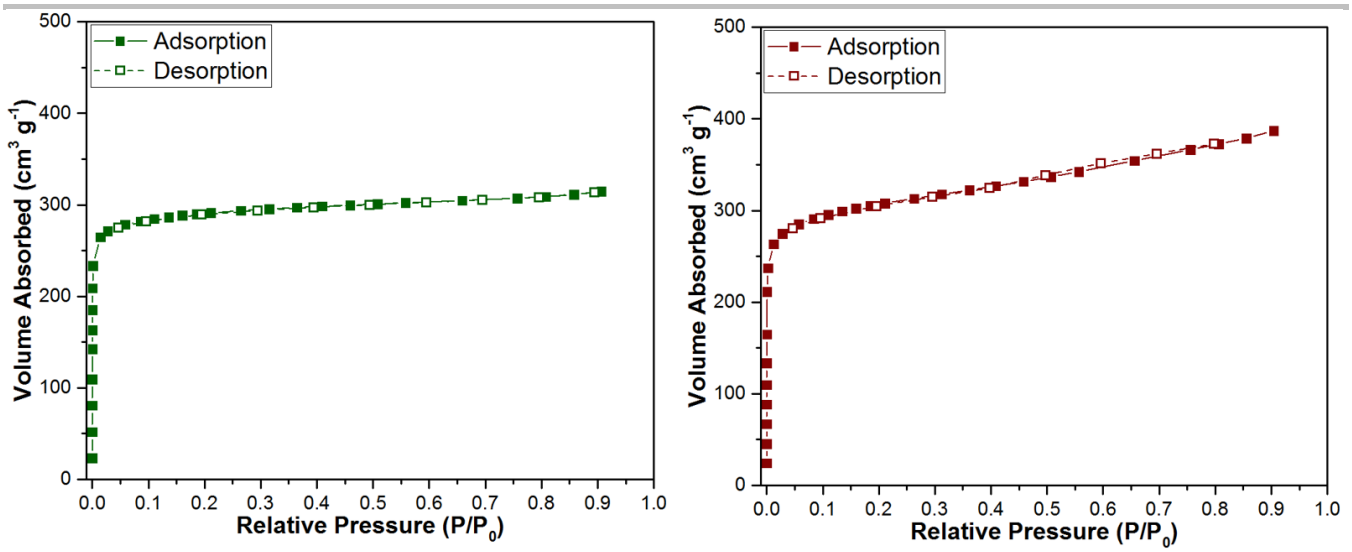

Figure S14. N_2 adsorption-desorption isotherm of 9.2 (± 0.4) wt% Ni_2P/MIL-125-NH_2, before (Left) and after (Right) recycling experiments with a BET surface areas of 1196 $m^2 g^{-1}$ and 1150 $m^2 g^{-1}$, respectively and a mean pore diameter of 1.7 and 1.6 nm, respectively.

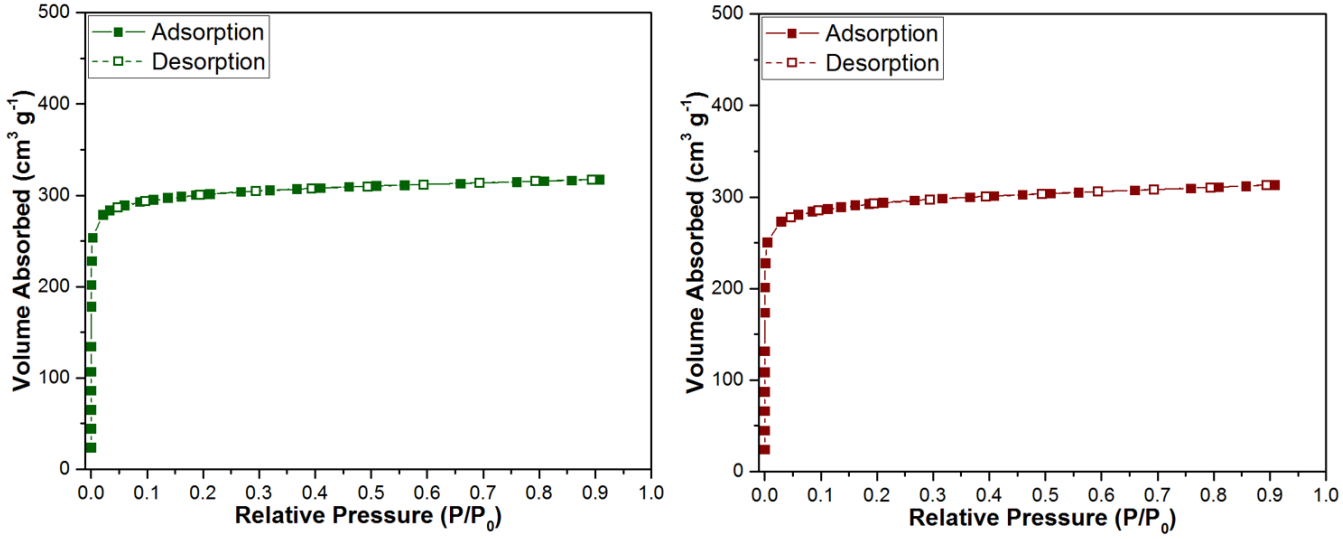

Figure S15. N_2 adsorption-desorption isotherm of 10.6 (± 0.4) wt% Ni_2P/MIL-125-NH_2, before (Left) and after (Right) photocatalysis with a BET surface areas of 1172 $m^2 g^{-1}$ and 1158 $m^2 g^{-1}$, respectively

S9. Calculation of Apparent Quantum Yield

S9.1 Moles of photons emitted by the xenon lamp

The moles of photons emitted by the xenon lamp at 400 nm and 450 nm was calculated by means of **Ferrioxalate actinometry**: [4, 5]

Stock solutions were prepared using Millipore water: **0.40 M Iron (III) stock solution** (**1**) was prepared by dissolving 4.025 g Iron(III) nitrate nonahydrate ($Fe(NO_3)_3 \cdot 9H_2O$) in 20.0 mL of water. This was acidified with 1.375 mL Sulfuric acid (H_2SO_4), and made up to 25 mL with additional water. **1.20 M Di-potassium oxalate stock solution (2)** was prepared by adding 4.975 g di-potassium oxalate monohydrate ($K_2C_2O_4$) to 25.0 mL of water. **Phenanthroline/buffer solution (3)** was prepared by dissolving 0.025g anhydrous 1,10-Phenanthroline ($C_{12}H_8N_2$) and 5.625g Sodium Acetate Trihydrate ($NaCH_3COO \cdot 3H_2O$) in 20.0 mL of water. 1.22 mL Sulfuric acid (H_2SO_4) was added and the solution made up to 25.0 mL with additional water.

The reaction solution was prepared by adding 1.70 mL of solution (**1**) and 1.70 mL of solution (**2**) with 30.6 mL of water in the dark. After stirring, 17.0 mL of the solution was transferred into a reactor (reactor **A**) which was irradiated by a 300 W Xe lamp equipped with a monochromatic filter (400 or 450 nm) for 46 min, while the remaining 17 mL was kept in the dark (reactor **B**). 0.5 mL of sample from reactor (A) was extracted, and added 1.0 mL of solution (**3**), and made up to 5.0 mL with water. 0.5 mL of sample from reactor B was treated the same. UV-Vis absorbance (400-600 nm) was recorded for both samples, with the difference in absorbance between the two recorded at 510 nm.
The moles of Fe^{2+} were calculated by using the formula:

$$n_{Fe(II)} = \frac{V_1 \cdot V_3 \cdot \Delta A}{10^3 \cdot V_2 \cdot L \cdot \varepsilon}$$

V_1: irradiation volume, V_2: sample taken, V_3: final volume, L: optical path-length, ΔA absorbance difference at 510 nm, ε: absorbance coefficient.

From this, the number of photons per min was calculated using the formula:

$$\frac{n_{photons}}{min} = \frac{n_{Fe(II)}}{\Phi_\lambda \cdot t \cdot F}$$

Φ_λ: Quantum yield for iron production at wavelength λ, t: time, F: mean fraction of light absorbed

Calculation:

$$n_{Fe(II)} = \frac{V_1 \cdot V_3 \cdot \Delta A}{10^3 \cdot V_2 \cdot L \cdot \varepsilon}$$

Where:

V_1: irradiation volume (17.0 mL)

V_2: sample taken (0.5 mL)

V_3: final volume (5.0 mL)

L: optical pathlength (1.0 cm)

ΔA absorbance difference at 510 nm

- At 450 nm irradiation : ΔA_1= 0.870758, ΔA_2= 0.892268
- At 400 nm irradiation : ΔA_1= 1.688539, ΔA_2=1.775813

ε: molar extinction coefficient (11100 L mol^{-1} cm^{-1})

- Moles of Iron(II) at 450 nm irradiation :

  1st measurement $n_{Fe(II)} = 1.36654\ 10^{-5}$

  2nd measurement $n_{Fe(II)} = 1.33359\ 10^{-5}$

- A Moles of Iron(II) at 400 nm irradiation :

  1st measurement $n_{Fe(II)} = 2.58605\ 10^{-5}$

  2nd measurement $n_{Fe(II)} = 2.71971\ 10^{-5}$

$$\frac{n_{photons}}{min} = \frac{n_{Fe(II)}}{\Phi_\lambda \cdot t \cdot F}$$

Φ_λ: Quantum yield for iron production at at wavelength λ
(1.14 at ~405 nm and 1.11 at ~450 nm)

t: time (46 min)

F: mean fraction of light absorbed = 1

- At 450 nm : $\frac{\bar{n}_{photons}}{min} = 2.64408\ 10^{-7}$
- At 400 nm : $\frac{\overline{n}_{photons}}{min} = 5.1713\ 10^{-7}$

S9.2 Moles of hydrogen generated under 400 nm and 450 nm radiation

The amount of hydrogen generated under 400 nm radiation was carried out using the same reaction mixture and setup as the photocatalytic experiments (S10) with the exception of using a 400 nm or 450 nm band pass filter with the xenon lamp.

- At **450 nm** Amount of H_2 for $Ni_2P/MIL\text{-}125\text{-}NH_2$:
  2.0937 10^{-6} mol in 240 min (4 h)

- At **400 nm** Amount of H_2 for $Ni_2P/MIL\text{-}125\text{-}NH_2$:
  5.44937 10^{-5} mol in 780 min (13 h)

- At **400 nm** Amount of H_2 for Ni_2P/TiO_2:
  6.77113 10^{-7} mol in 300 min (5 h)

S9.3 Apparent quantum yield (AQY) determination

The apparent quantum yield was calculated by using the following formula: $$\mathrm{AQY}(\%) = \frac{2\frac{\mathrm{N\,H_2}}{\mathrm{min}}}{\frac{\mathrm{N\,photons}}{\mathrm{min}}} 100$$

Where $\frac{N\ H_2}{min}$ = number of hydrogen molecules evolved per minute,

and $\frac{N\ photons}{min}$ = number of incident photons per minute.

Calculation:

- **Ni_2P/MIL-125-NH_2**:

AQY = 27.0 % and 6.6 % at 400 and 450 nm respectively.

- **Ni_2P/TiO_2**:

AQY = 0.873 % (0.9 %) at 400 nm.

S10. Comparison of Ni_2P/MIL-125-NH_2 with Ni_2P/TiO_2 under UV-vis radiation

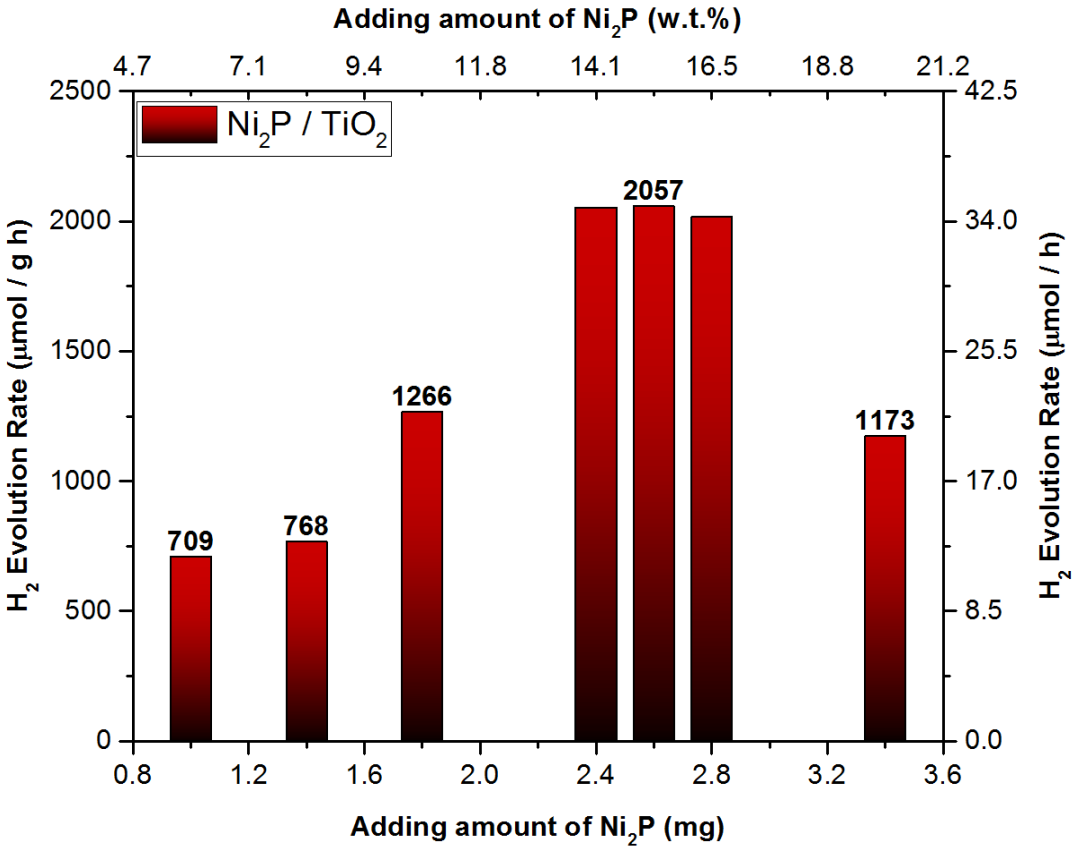

Figure S16. H_2 evolution rate of 17.0 mg TiO_2 against different adding amounts of Ni_2P NPs, in a 17.0 mL acetonitrile-based solution of 16.4 V/V% TEA and 1.64 V/V% Water.

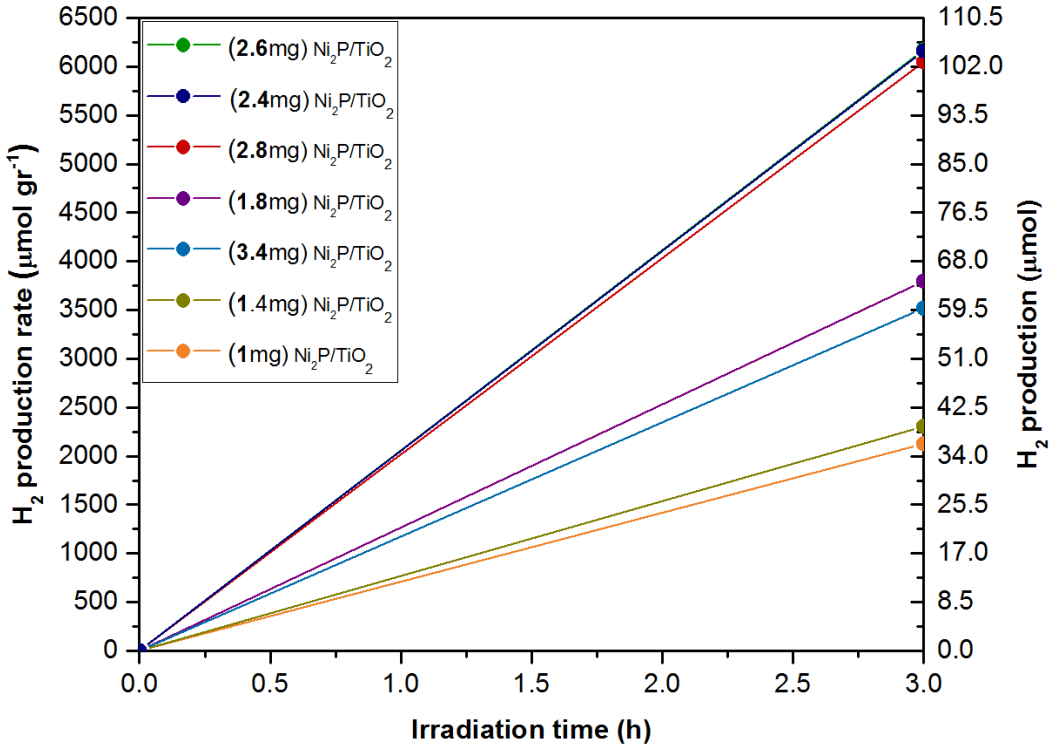

Figure S17: Photocatalytic Hydrogen production of 17.0 mg TiO_2 with different adding amounts of Ni_2P NPs – to optimize the conditions and identify the ratio for best performing system.

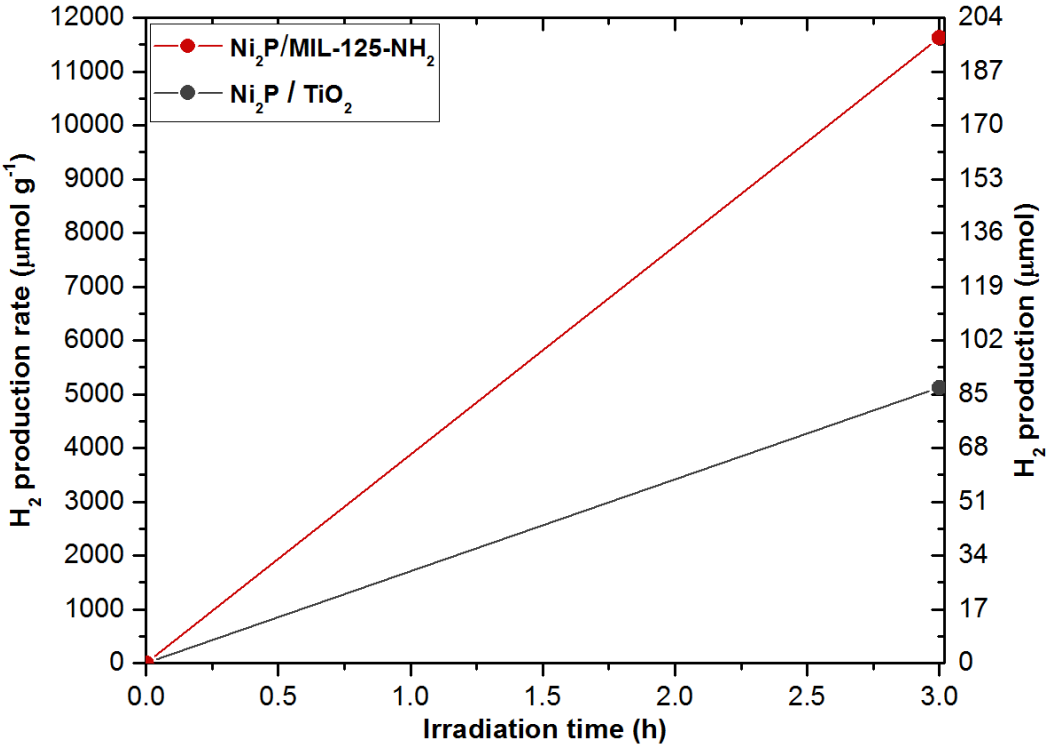

Figure S18. Photocatalytic performance towards H_2 evolution of optimized 15.3 (± 0.4) wt% Ni_2P/TiO_2 and 9.2 (± 0.4) wt% Ni_2P/MIL-125-NH_2, under UV-Vis light irradiation. Conditions: 1.56 (± 0.06) mg and 2.6 (±0.06) mg of Ni_2P NPs in 17.0 mg of MOF and TiO_2 respectively, in a 17.0 mL acetonitrile-based solution of 16.4 V/V% TEA and 8.2 V/V% Water.

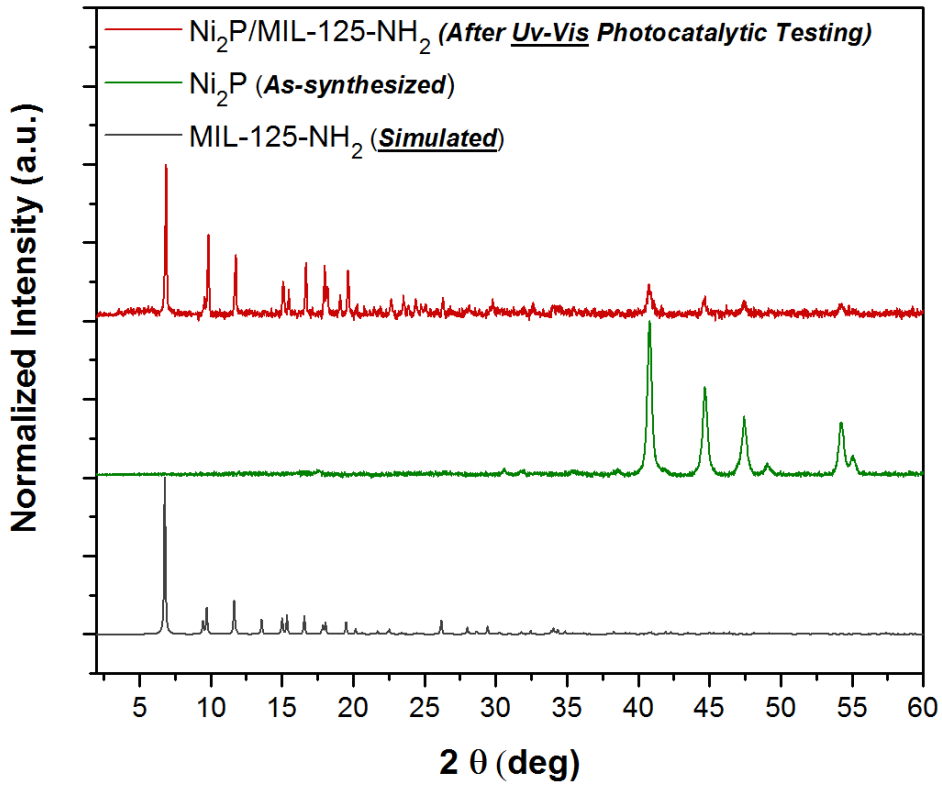

Figure S19. Powder X-ray diffraction patterns of MIL-125-NH_2 simulated (dark gray), Ni_2P as-synthesized (green) and 9.2 (± 0.4) wt% Ni_2P/MIL-125-NH_2 after 3 h of photocatalytic test under UV-Vis irradiation.

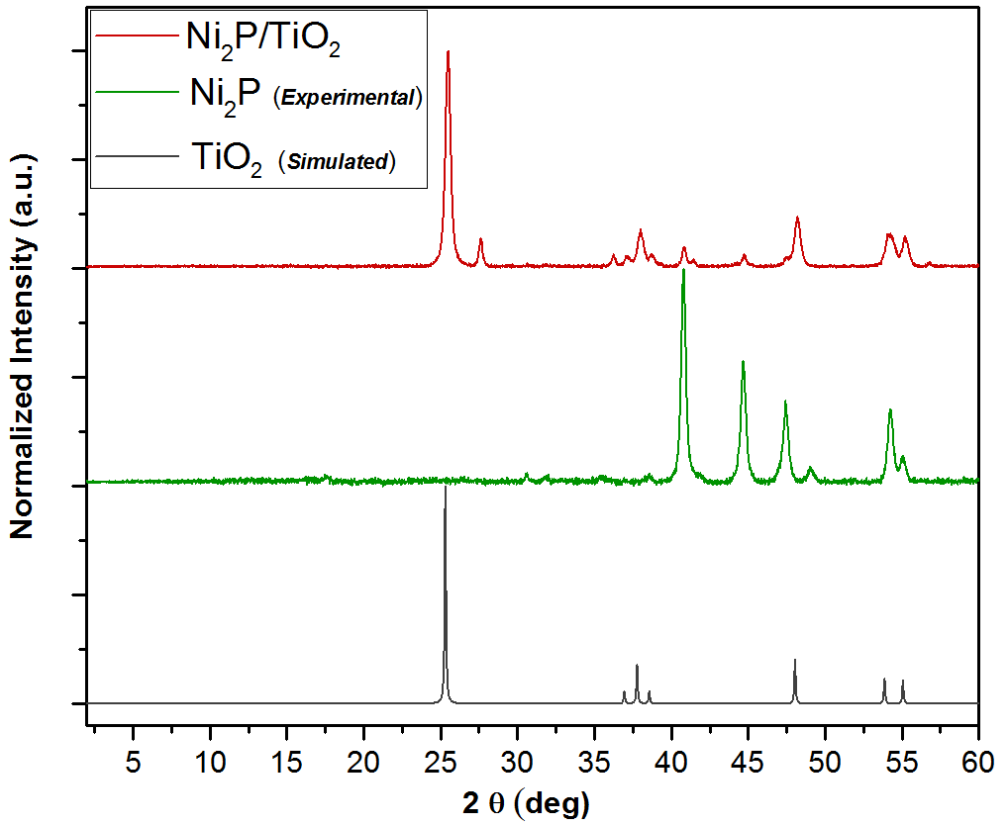

Figure S20. Powder X-ray diffraction patterns of TiO_2 simulated (dark gray), Ni_2P as-synthesized (green) and 15.3 (± 0.4) wt% Ni_2P/TiO_2 after 3 h of photocatalytic test under UV-Vis irradiation.

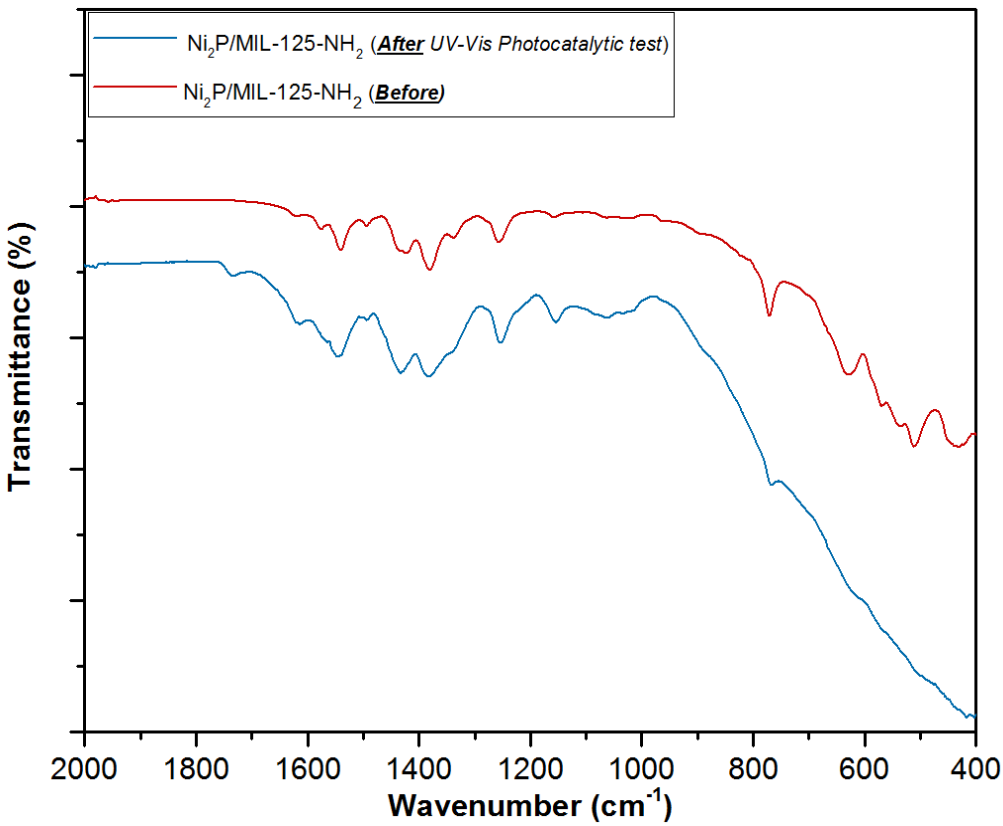

Figure S21. FTIR spectra of $Ni_2P/MIL\text{-}125\text{-}NH_2$ before (red) and after (blue) photocatalytic test under UV-Vis irradiation showing that MIL-125-NH2 does not collapse as shown by the similarity between the two spectra.

S11. Density functional theory (DFT) calculations

Density Functional Theory calculations have been performed using the CP2K computational chemistry package.[6] We calculated the electronic structure employing the PBE GGA exchange and correlation functional,[7] the Goedecker-Teter-Hutter pseudopotential with a cut-off of 700Ry,[8] and the DZVP-MOLOPT basis set for H, C, O, and N atoms and the short range TZVP-MOLOPT basis set for Ti atoms.[9]

After ground state relaxation of the MIL-125 system, we added random -NH_2 groups and re-optimized by keeping the cell parameters constant. Injection of the charge-carriers was simulated by adding an extra electron or an extra hole to the system, followed by optimization of the structure. In Fig. S20 left, we report the spin density of the system (pink) after electron injection. The spin-density distribution shows that the electron, after geometrical reorganization, is delocalized along two opposed ligand bridges connecting the Ti-oxo cluster of different planes. Such delocalization is a key element for ensuring electron mobility within the MOF in its excited state. After photo-generation, the electron can be transported to the external surface of the MOF crystal, where it can be transferred to the co-catalyst. After photoexcitation, the hole is localized over the organic ligand, in aniline π orbitals, as shown by the spin density distribution (green) plotted in Fig. S20 right. The localization of the hole occurs over a plane that it is perpendicular to the direction of the electron delocalization. This decreases the probability of charge-carrier recombination, and thus, of relaxation into the electronic ground state.

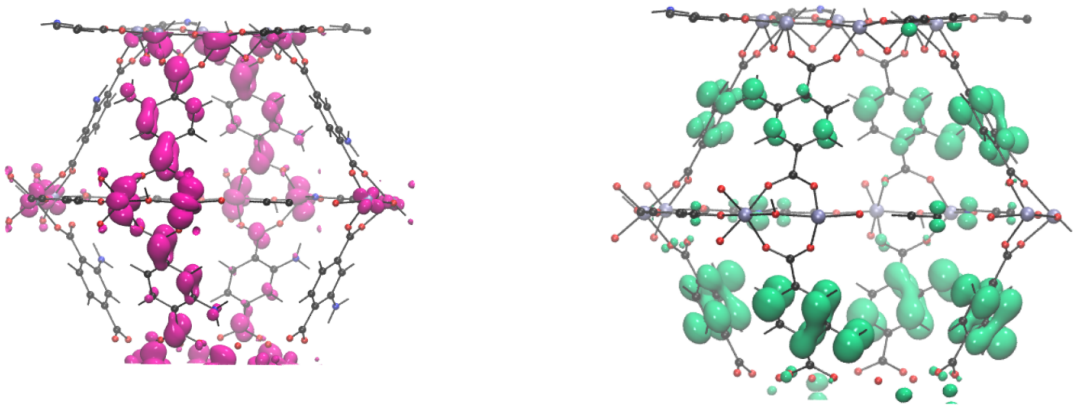

Figure S22. Spin density distribution in MIL-125-NH_2 (Left): after electron injection (Right): after hole injection. the pink spheres represent the difference in spin density distribution after electron addition, while the green shapes represent the same after electron removal, thus indicating the potential location of a photogenerated electron and hole. Atom color code: Carbon: black, Oxygen: red, Nitrogen: blue, Titanium: light purple.

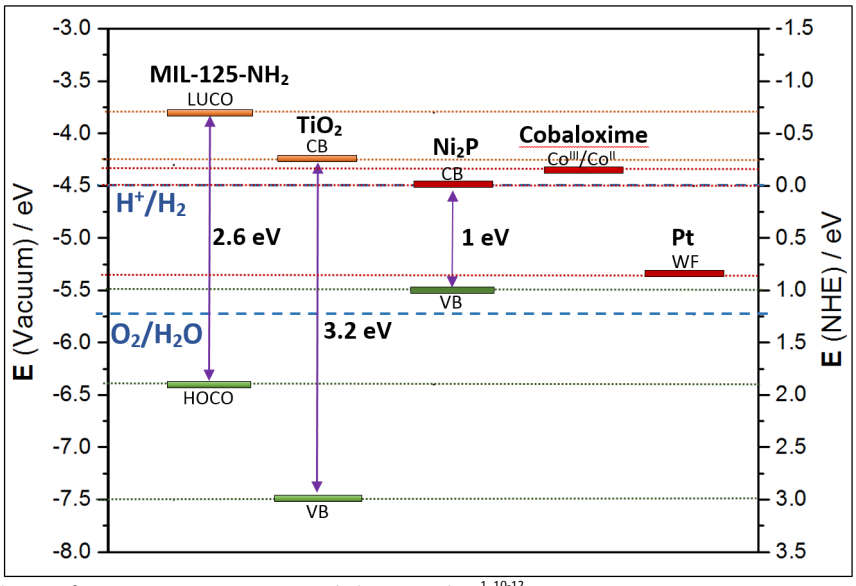

Figure S23. Energy diagram for MIL-125-NH_2, TiO_2, Ni_2P, cobaloxime and Pt.[1, 10-12]

S12. Electron paramagnetic resonance (EPR)

To investigate the mechanistic aspects of hydrogen generation catalyzed by Ni_2P/MIL-125-NH_2, electron paramagnetic resonance (EPR) studies were performed. In particular, low-temperature EPR (LT-EPR) measurements were carried out using a Bruker EleXsys E500 X-band (9.4 GHz) EPR spectrometer (Bruker BioSpin GmbH, Karlsruhe, Germany), which was equipped with a high-Q cylindrical cavity, Model ER 4122 SHQE, and a helium gas-flow cryostat, ESR900 (Oxford Instruments Ltd., Tubney Woods, Abington, England). At cryogenic temperatures, the sample temperature was stabilized and monitored by an ITC503 temperature controller (Oxford Instruments Ltd.). In this study, all spectra were acquired at 20 K.

Three samples Ni_2P, MIL-125-NH_2, and the mixture of Ni_2P/MIL-125-NH_2 were subjected to LT-EPR measurements. The liquid samples were filled into the bottom-sealed thin-walled quartz capillaries (VitroCom Inc. tubes, Model CV2024Q, 2.4 mm OD/2.0 mm ID, 100 mm length), which were then transferred into the standard EPR quartz tubes (Wilmad-LabGlass Inc., Model 707-SQ-250M, 4.0 mm OD/3.0 mm ID, 250 mm length).

Prior to perform LT-EPR measurements, in order to prevent the presence of oxygen and provide good thermal contact at cryogenic temperatures, pure helium gas was blown into the EPR tubes. Subsequently, the prepared samples were rapidly frozen at 77 K and transferred into the pre-cooled (20 K) insert of the helium gas-flow cryostat of the EPR spectrometer. The sample volume placed into the EPR resonator was of *ca.*100 µL. The typical instrumental settings were: sweep width 10000 G (1.0 T); magnetic field modulation frequency 100 kHz; magnetic field modulation amplitude 5.0 G (0.5 mT); lock-in time constant 20.48 ms; lock-in integration time 81.92 ms; number of points per scan 4096; resulting sweeping time 335.54 sec; typical microwave frequency ~9.4 GHz; microwave power 0.63 mW; per each EPR spectrum two scans were accumulated.

The LT-EPR spectra recorded after the exposure of the samples to the visible light illumination for 20 min (halogen, 150 W) are shown in **Figure 2**. For MIL-125-NH_2, the central EPR feature having the *peak-to-peak* width of 92 G and centered at $\boldsymbol{g_{ave}}$~1.930 can be assigned to Ti^{3+}. Similar spectra have frequently been reported in reduced nano-particular rutile or anatase TiO_2 and associated with the occurrence of Ti^{3+} paramagnetic centers.[13, 14] Recently, a similar EPR feature assigned to Ti^{3+} has been reported for Ti-containing MOFs. [15, 16] In addition, the EPR spectrum of MIL-125-NH_2 shown in **Figure 2** also display a second feature, although markedly weaker, having relatively well-resolved ***g***-tensor components, $\boldsymbol{g}_{zz}$ = 2.035, $\boldsymbol{g}_{yy}$ =2.012, and $\boldsymbol{g}_{xx}$ = 2.0057. The presence of this EPR signal provides evidence for the formation of superoxide radicals ($O_2^{\bullet-}$).[17, 18] The LT-EPR spectrum of Ni_2P/MIL-125-NH_2 recorded after the exposure to the visible light illumination for 20 min (halogen, 150 W) is shown in **Figure 2**. The central EPR feature having the *peak-to-peak* width of 180 G and centered at $\boldsymbol{g_{ave}}$~2.0097 can be assigned to paramagnetic centers of Ni^+ (d^9, ***S***=1/2) created by light-induced electron transfer from MIL-125-NH_2 to the otherwise EPR-silent Ni_2P. Although nickel (I) compounds are frequently thermally unstable and the corresponding literature reports on EPR detection of Ni^{1+} paramagnetic centers are quite rare, recently, similar spectra have been reported for carbene-nickel complexes.[19]

In conclusion, the LT-EPR measurements confirms the light-induced reduction of Ti^{4+} to Ti^{3+} and Ni^{2+} to Ni^+ for the samples MIL-125-NH_2 and Ni_2P/MIL-125-NH_2, respectively.

LT-EPR measurements were also performed for Pt NPs and Pt/MIL-125-NH_2 mixture; the corresponding spectra are shown in **Figure S22**. However, as can be seen, no EPR signals were observed for both samples. We believe that the lack of conduction electron spin resonance (CESR) signals for $Pt^{\delta-}$ NPs can be related to a possible mobility of these nanoparticles and formation of larger metallic clusters. For bigger agglomeration of $Pt^{\delta-}$ NPs, like for bulk metals, the spin relaxation mechanism is dominated by the extremely efficient spin-orbit coupling, which leads to very short relaxation times. As a result, the CESR features are very broad, thus making their detection difficult, even at cryogenic temperatures.

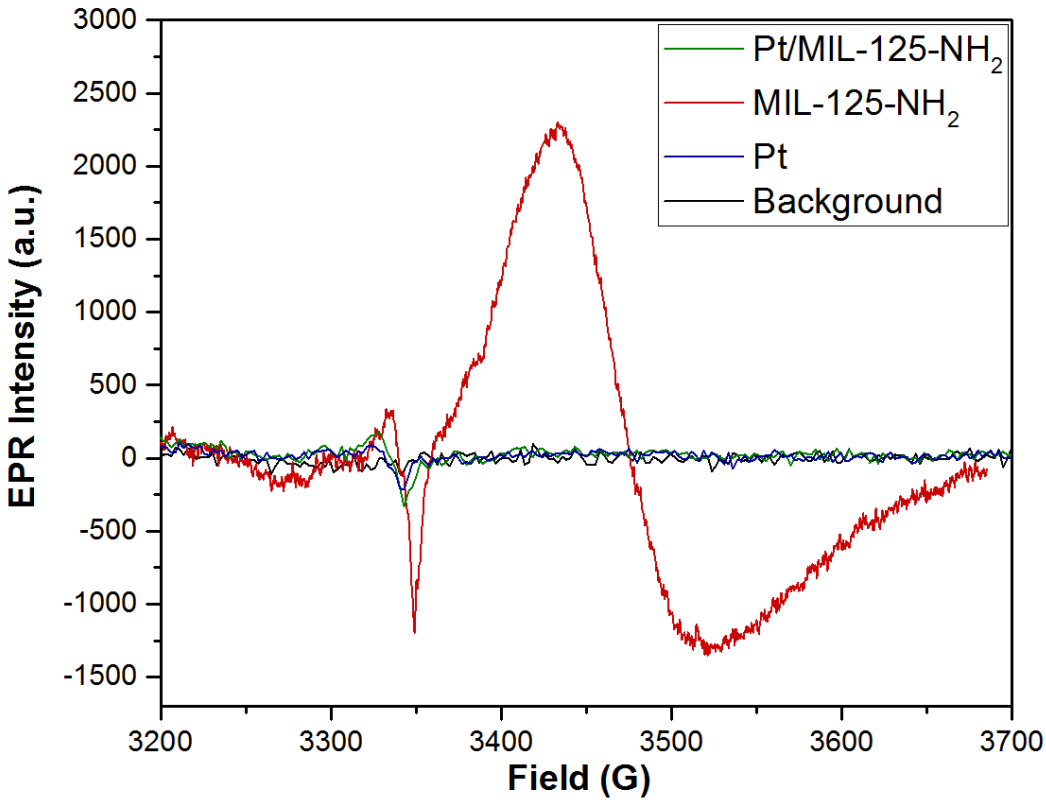

Figure S24. EPR spectra of Pt/MIL-125-NH_2 (green), MIL-125-NH_2 (red), Pt (blue) after visible light irradiation.

S13. Inductively coupled plasma optical emission spectrometry (ICP-OES)

In order to investigate the interactions between the MIL-125-NH_2 and the Ni_2P nanoparticles (NPs), ICP-OES measurements were performed using a NexIon 350 (Perkin Elmer) spectrometer.

We prepared two CH_3CN-TEA-H_2O solutions (17.0 mL); the first one is with 1.56 (± 0.06) mg of dispersed Ni_2P NPs, while the second one contains 1.56 (± 0.06) mg of Ni_2P NPs and 17.0 mg of the MIL-125-NH_2. Both solutions were initially sonicated and then left undisturbed for 40 minutes; 1.0 mL of each solution was collected and dried in air. Subsequently, 4.0 mL of Nitric acid were added in each sample to completely dissolve the powders and the resulting solutions were subjected to ICP-OES experiments. The concentrations of Ni in the two samples are shown in Table S1. In the solution containing only Ni_2P NPs, the concentration of Ni is 17.5 ppm, which is close to the expected concentration of 17 ppm. This concentration is much higher than the one in the solution containing the mixture of Ni_2P NPs and MIL-125-NH_2, illustrating that ~90% Ni_2P NPs were attached on the external surface of the MOF.

We repeated the exact same procedure for Pt NPs. Interestingly, ICP-OES shows that by simply mixing the Pt NPs with MIL-125-NH_2, less than 40% Pt NPs were attached on the MOF, demonstrating that the Ni_2P are better deposited on the MIL-125-NH_2.

Table S1: Concentration of Ni and Pt in solution with and without the MIL-125-NH_2.

	Ni in solution of Ni_2P NPs	**Ni** in solution of Ni_2P/ MIL-125-NH_2	**Pt** in solution of Pt NPs	**Pt** in solution of Pt/ MIL-125-NH_2
Concentration (ppm)	**17.5**	**2.0**	**5.2**	**3.2**

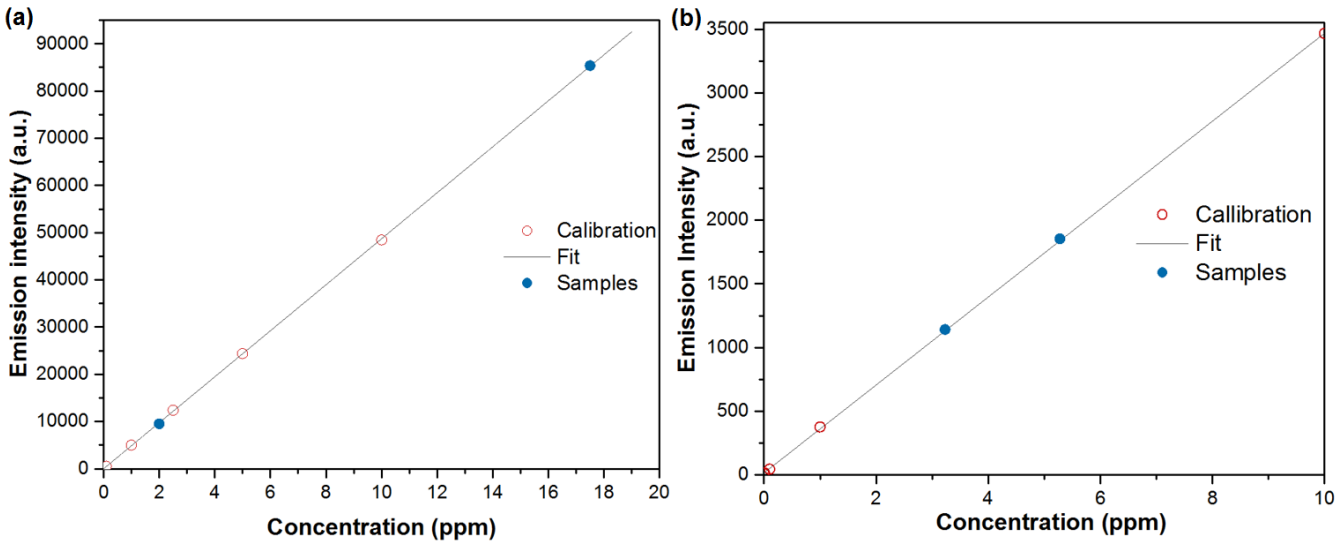

Figure S25. a) Concentrations of Ni and b) of Pt from ICP-OES measurements.

S14. Comparison of the photocatalytic activity of Ni_2P/MIL-125-NH_2 with other systems

S14.1 Ni_2P/MIL-125-NH_2 in 0.01 M TEOA aqueous solution

We tested the photocatalytic performance of the Ni_2P/MIL-125-NH_2 in a 0.01 M TEOA aqueous solution and after 3 h of operation we observed that the MIL-125-NH_2 collapses.

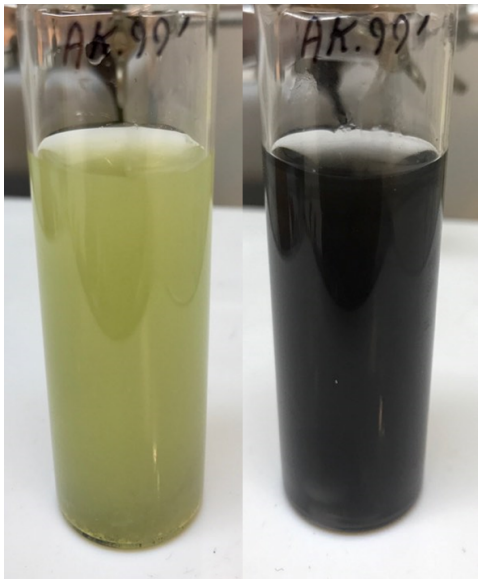

Figure S26. Ni_2P/MIL-125-NH_2 before (left) and after (right) 3h photocatalytic testing in a 0.01 M TEOA aqueous solution under visible irradiation.

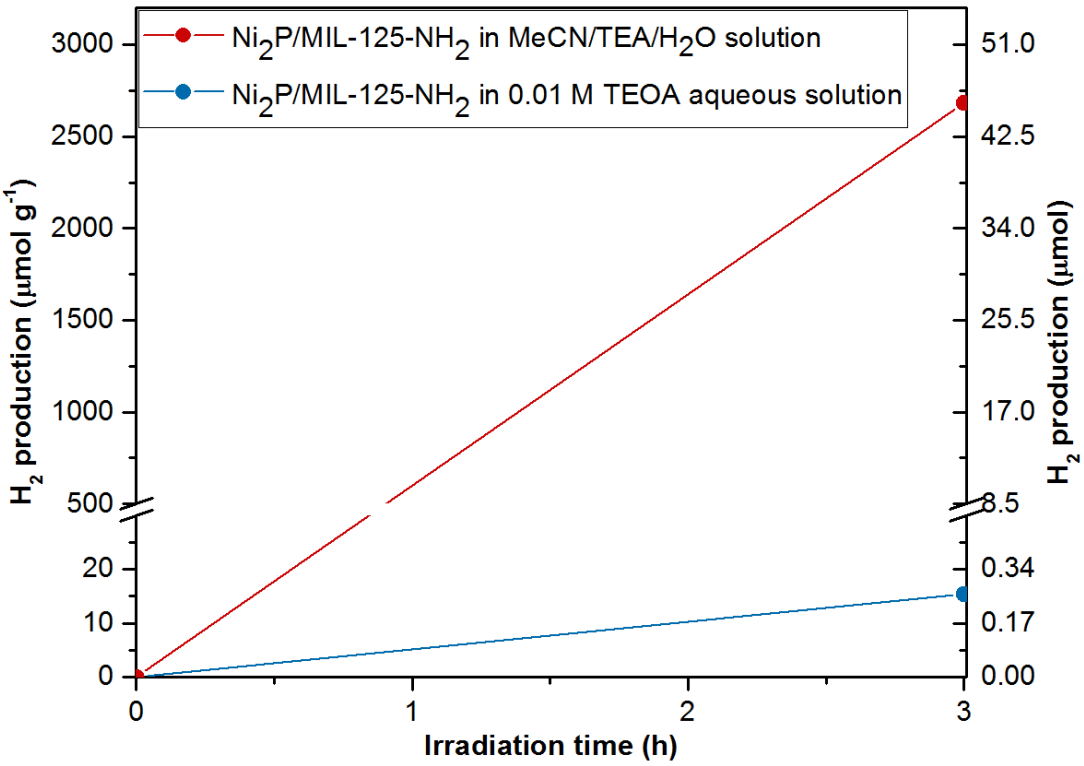

Figure S27. Photocatalytic performance towards H_2 evolution of optimized 9.2 (± 0.4) wt% Ni_2P/MIL-125-NH_2 in 2 different photocatalytic solutions under Visible light irradiation. Photocatalytic solution 1 (red): 17.0 mL acetonitrile-based solution of 16.4 v/v% TEA and 4.87 v/v% Water. Photocatalytic solution 2 (blue): 17.0 mL of 0.01 M TEOA aqueous solution.

S14.2 Comparison of Ni_2P/MIL-125-NH_2 with Pt/MIL-125-NH_2

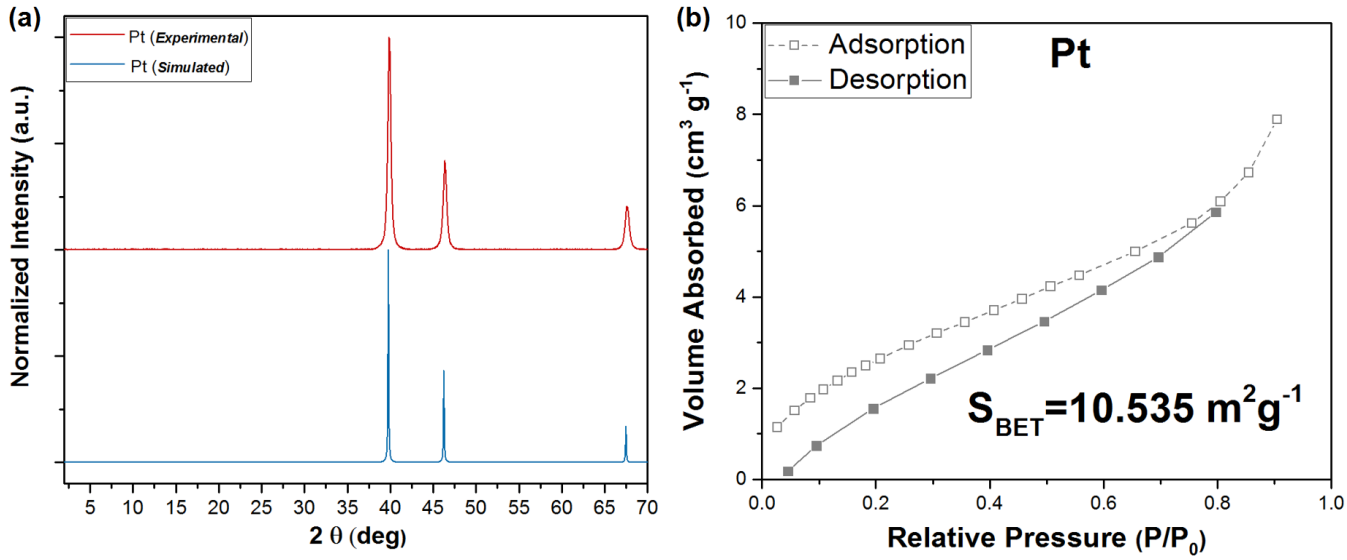

Figure S28. (a) Powder X-ray diffraction pattern of simulated (blue) and as-synthesized (red) Pt NPs, (b) N_2 adsorption-desorption isotherm of Ni_2P NPs.

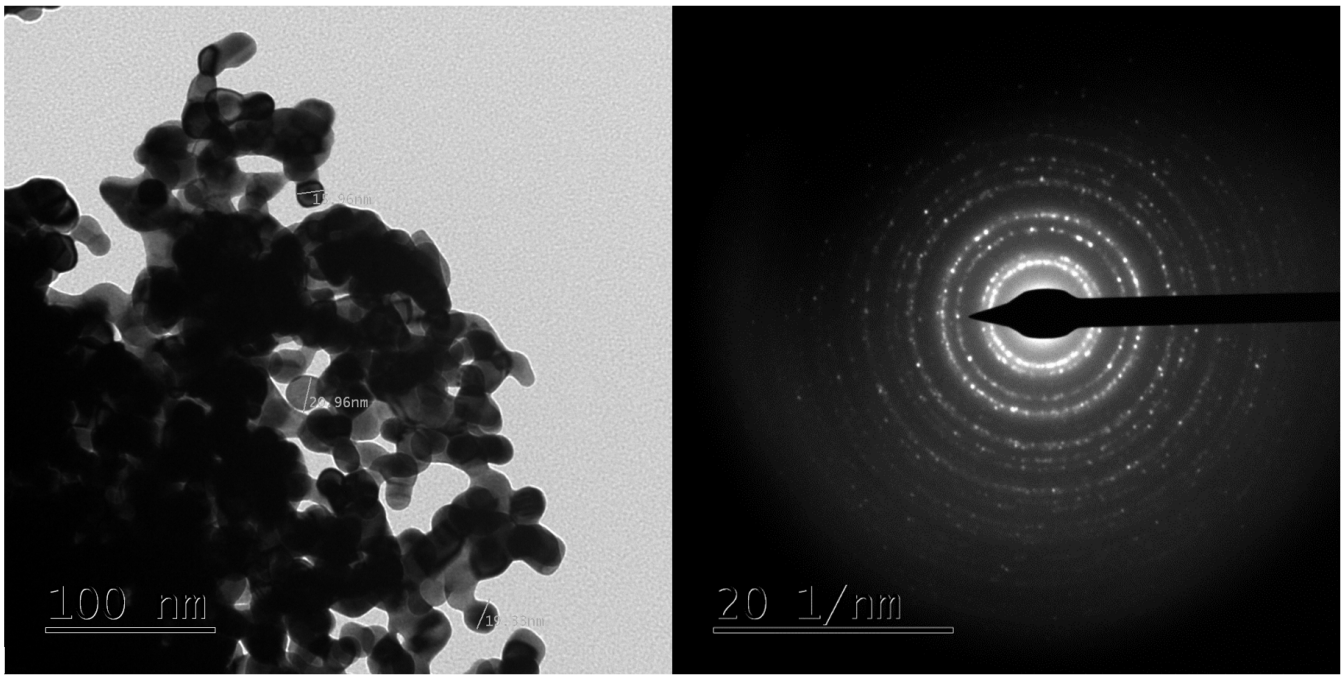

Figure S29. (a) TEM image, and (b) Electron Diffraction pattern of Pt NPs. The size of Pt NPs is estimated to be around 20 nm.

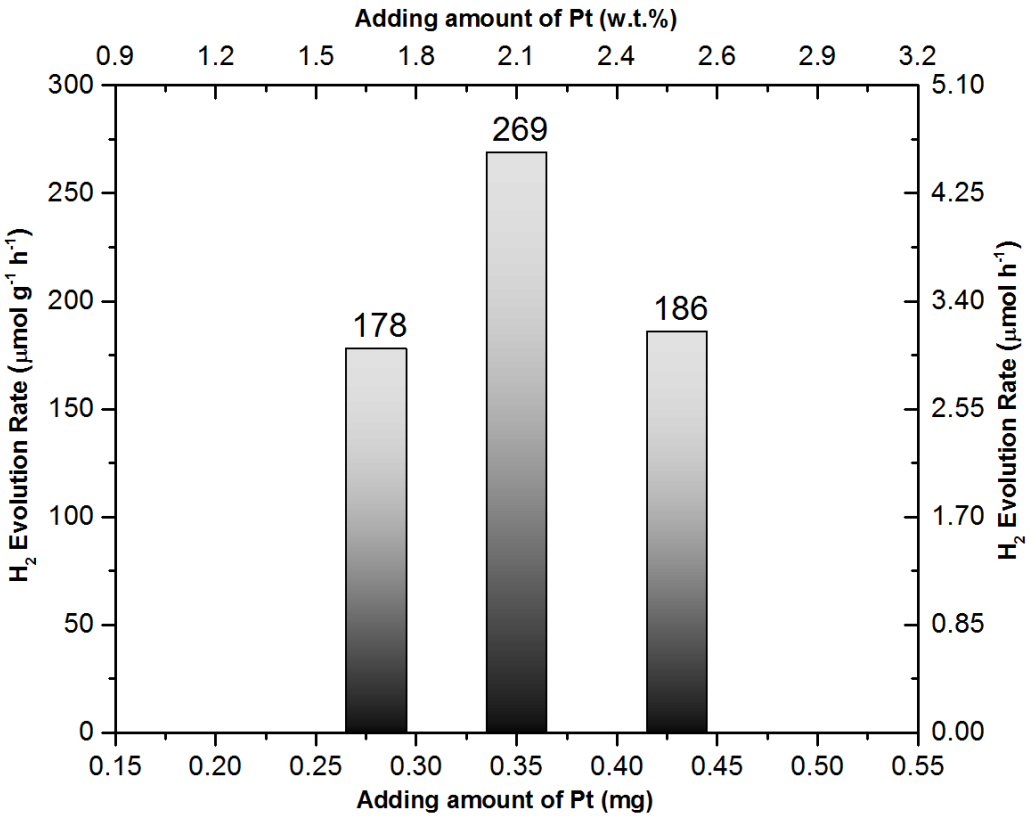

Figure S30. H_2 evolution rate of 17.0 mg MIL-125-NH_2 against different adding amounts of Pt NPs.

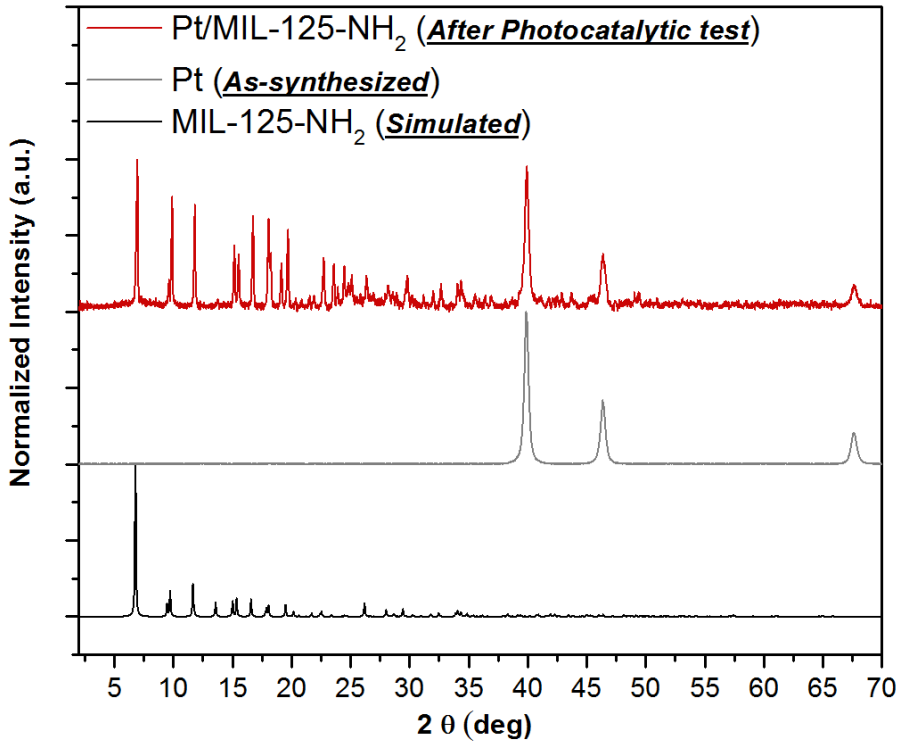

Figure S31. Powder X-ray diffraction patterns of MIL-125-NH_2 simulated (dark gray), Pt NPs as-synthesized (light gray) and 2 (± 0.4) wt% Pt/MIL-125-NH_2 after photocatalytic test. This shows that Pt NPs are present with MIL-125-NH_2 after photocatalysis.

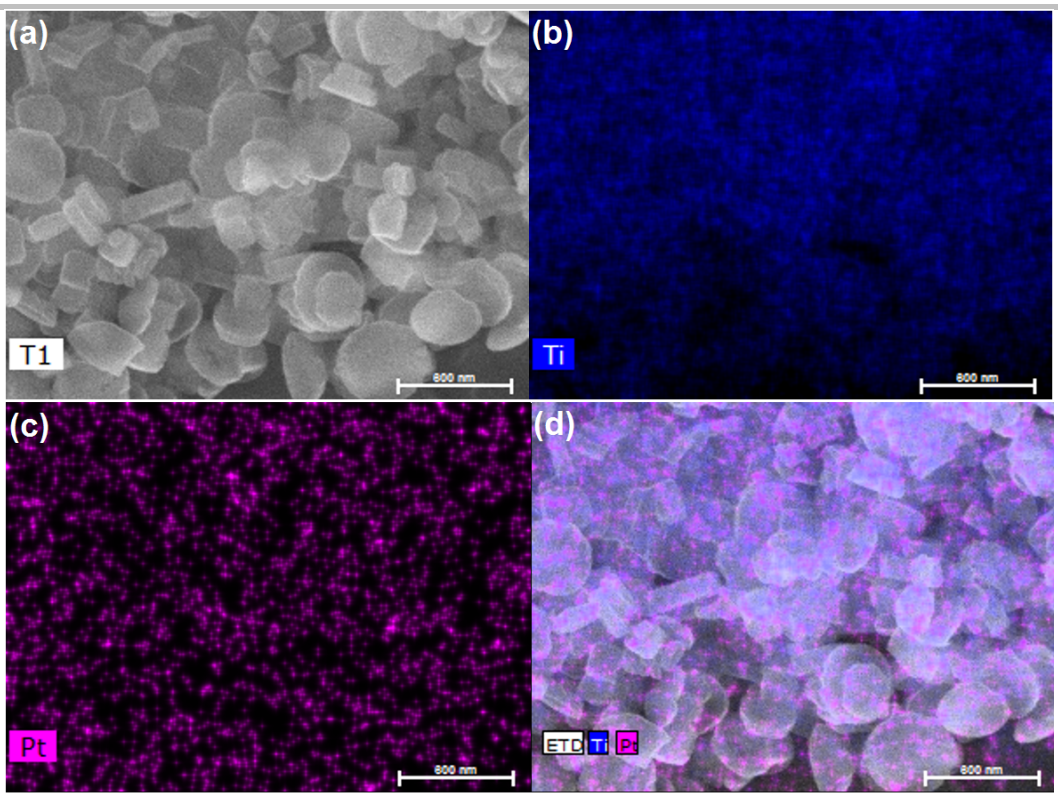

Figure S32. (a) SEM image of 2 (± 0.4) wt% Pt/MIL-125-NH_2 after photocatalytic testing, and corresponding EDX maps of (b) Titanium, (c) Pt and (d) both Ti and Pt.

S15. Photoelectrochemical Chronoamperometry measurements

To perform the photoelectrochemical measurements a MIL-125-NH_2 thin film was deposited on fluorine-doped SnO_2 (FTO) glass as conductive substrate. To do so, 10 mg of MIL-125-NH_2 was mechanically ground with 20 µL of nafion and 2 mL of ethanol. Subsequently the resulting suspension was drop-casted on FTO glass (30 µL cm^{-2}) and dried in the air.

The chronoamperometry measurements were performed in a three-electrode configuration "Cappuccino"-type cell with the MIL-125-NH_2 thin-film electrode as the working electrode, a Pt wire as counter electrode and a Ag/Ag^+ reference electrode. In all the cases an acetonitrile:water 96:4 (v/v) solution containing tetrabutylammonium perchlorate (TBAP, 1M), with increasing amounts of dispersed co-catalyst (Pt or Ni_2P nanoparticles) was employed as electrolyte. All the experiments were carried out under an applied potential of -0.6 V vs Ag/Ag^+, illuminating the samples with simulated 1 sun from the back-side (electrode-electrolyte side) to avoid parasitic light absorption from the electrolyte. The photocurrent response to ON and OFF states of light irradiation for the samples, in the presence Ni_2P or Pt nanoparticles are shown in Figure S31 and S32, respectively.

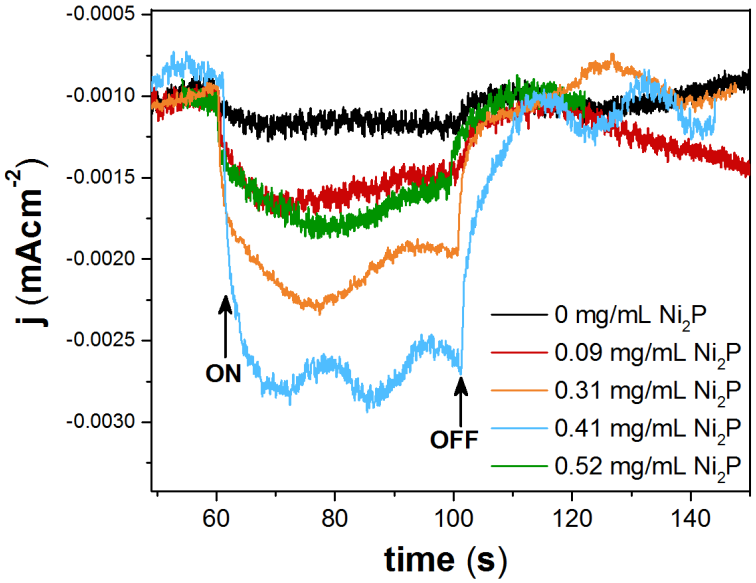

Figure S33. Photocurrent vs. time plot for the MIL-125-NH_2 thin-film electrode as a function of the amounts of dispersed nanoparticles of Ni_2P.

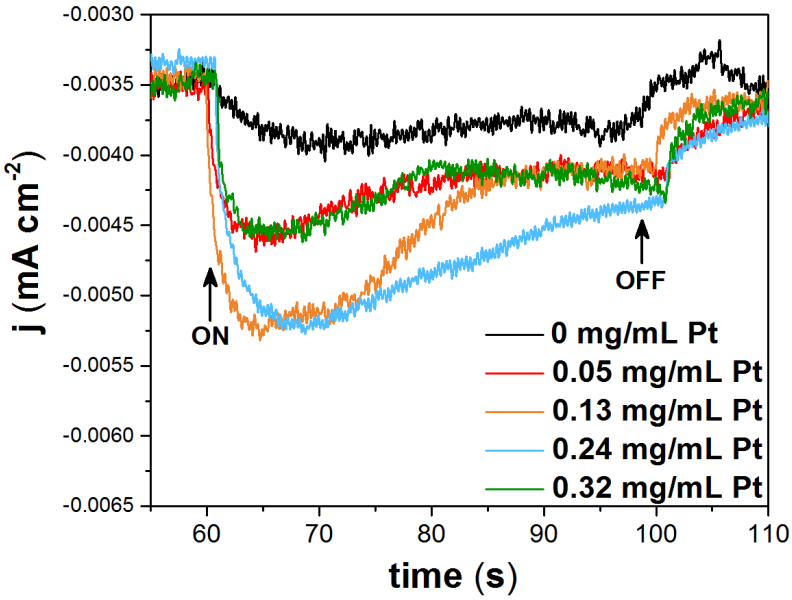

Figure S34. Photocurrent vs. time plot for the MIL-125-NH_2 thin-film electrode as a function of the amounts of dispersed nanoparticles of Pt.

Chronoamperometry measurements shown in **Figure 3** (in the main text) were performed at an applied potential of -0.6 V vs Ag/Ag^{+} using the adding amount of co-catalysts, that gave the highest photocurrents in previous experiments, but under stronger irradiance (2 suns) to increase the photocurrent with respect to the background current (to afford a better tracking of the differences over extended illumination periods). Note that both Ni_2P/MIL-125-NH_2 and Pt/MIL-125-NH_2 perform with comparable photocurrents at the early stage, but the photocurrent in the presence of Pt decays faster over time. This explains the differences observed in the photocatalytic experiments. Indeed, under steady-state operation in a particle-based photocatalytic measurement, the performance of the Pt/MIL-125-NH_2 system would reasonably be lower than that of Ni_2P/MIL-125-NH_2, due to the faster decaying performance of the MIL-125-NH_2 -Pt interaction compared to the MIL-125-NH_2 – Ni_2P interaction.

S16. Photoluminescence (PL) spectra

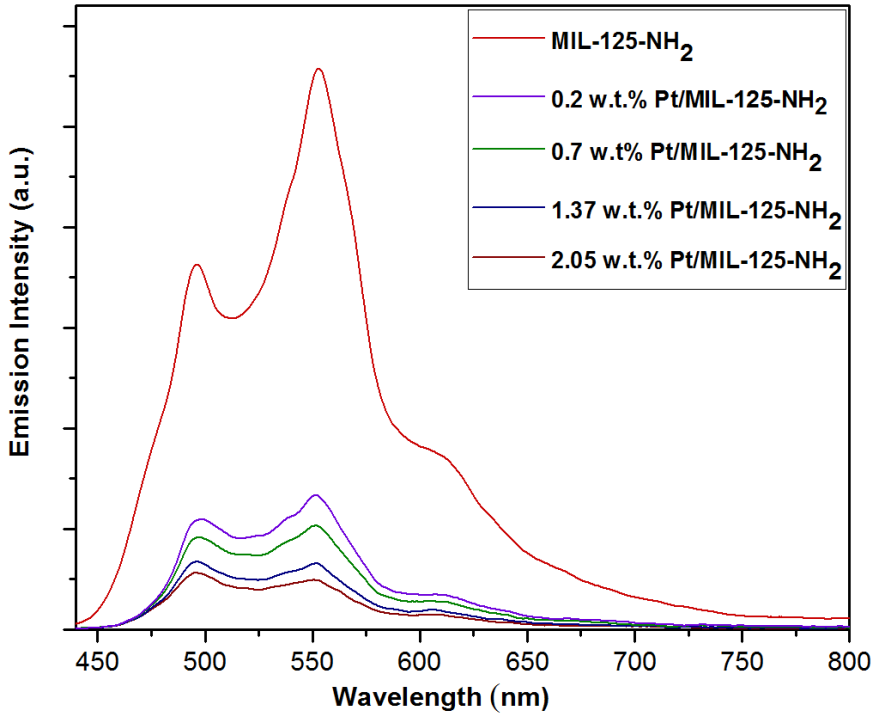

Figure S35. PL spectra (excited at 420 nm) for MIL-125-NH_2 and MIL-125-NH_2 with different adding amounts of Pt.

S17. Proposed mechanism for photocatalytic H_2 evolution

Upon visible light irradiation the MOF acts as a photosensitizer, subsequently an electron is excited from the HOCOs (Highest Occupied Crystalline Orbitals) to the LUCOs (Lowest Unoccupied Crystalline Orbitals). Then this electron is captured by the Ni_2P NPs which act as catalytic centers, reducing the hydrogen cations to dihydrogen.

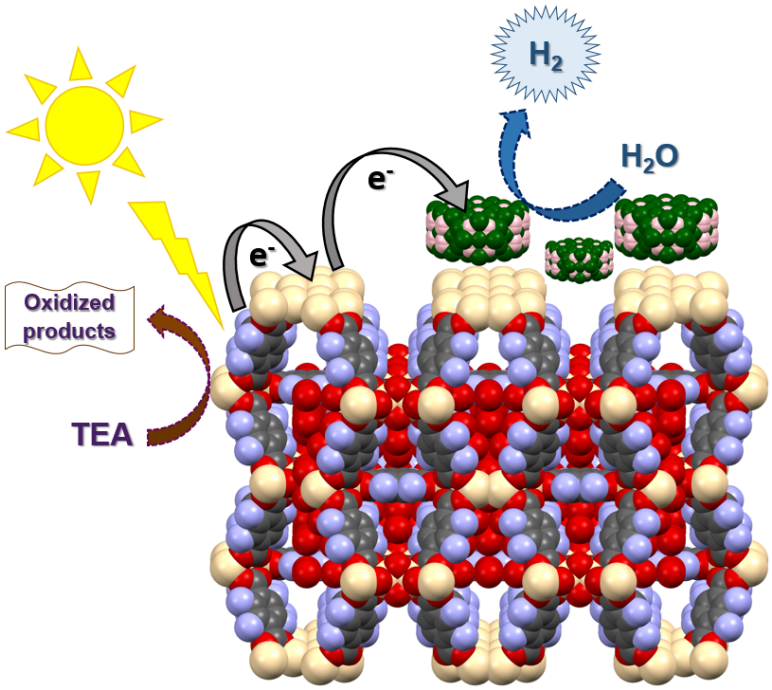

Figure S36. Schematic representation of charge transfer over Ni_2P/MIL-125-NH_2 under irradiation. Atom color code: Carbon: grey, Oxygen: red, Nitrogen: blue, Titanium: light yellow.

S18. Comparison of Ni_2P/MIL-125-NH_2 with literature

Table S2: Comparison of Ni_2P/MIL-125-NH_2 with current MOF-based hydrogen generation catalysts.

Photocatalyst	**Co-catalyst**	**Light Source** λ (nm)	**H_2 Evolution Rate** *with respect to the MOF*	**QY**	**Ref.**
MIL-125- NH_2 (Ti)	Pt Nps photodeposited	≥ 420	*333 μmol h^{-1} g^{-1}		[20]
Uio-66-NH_2 (Zr/Ti)	Pt Nps	≥ 420	3.5 mmol mol^{-1} in 5 h		[21]
Ti-MOF-Ru(tpy)$_2$	Pt Nps	≥ 420	*100-200 μmol h^{-1} g^{-1}	**AQY: 0.2** % at 500 nm	[22]
MIL-125-NH_2 (Ti)	Pt Nps photodeposited	≥ 420	*525 μmol h^{-1} g^{-1}		[23]
Al-PMOF	Pt Nps	≥ 420	200 μmol g^{-1} h^{-1}		[24]
Uio-66 (Zr)	2.87 w.t.% Pt	≥ 380	257.38 μmol h^{-1} g^{-1}		[25]
MIL-125(Ti)	Pt	≥ 320	*155 μmol h^{-1} g^{-1}		[26]
MIL-100 (Fe)	0.8 wt% Pt photodeposited	≥ 420	109 μmol h^{-1} g^{-1}		[27]
MOF-253 (Al)	Pt complex	≥ 420	100 μmol h^{-1}	**QE**: 1.63% at 440 nm	[28]
$[Cu(enMe)_2]_4[PNb_{12}O_{40}(VO)_6](OH)_5$ $6H_2O$	0.75% Pt	Hg lamp	43.86 μmol g^{-1} h^{-1}		[29]
$[Gd_2(abtc)(H_2O)_2(OH)_2]$ $2H_2O$	1.5 w.t.% Ag	Xe lamp	* 212 μmol h^{-1} g^{-1}		[25]
$Zr_6(\mu_3\text{-}O)_4(\mu_3\text{-}OH)_4(bpdc)_{5.94}$ $(L1)_{0.06}$	Pt Nps photodeposited	≥ 420	3400 turnovers after 48hrs	**AQY:** 3 x 10^{-4} % at 440 nm	[30]
UiO-66 (Zr)	Pt NPs in sol	Xe doped mercury	2.4 ml in 3hrs	**QY**: 0.1% at 370 nm	[31]
UiO-66-NH2 (Zr)	Pt NPs in sol	Xe doped mercury	2.8 ml in 3hrs	**QY**: 3.5% at 370 nm	[31]
UiO-66 (Zr) + Rhodamine B	Pt NPs on MOF	≥ 420	116 μmol h^{-1} g^{-1}		[32]
Uio-66 (Zr) + Erythrosin B	0.5 w.t.% Pt (photo-deposited)	≥ 420	*444 μmol h^{-1} g^{-1}		[33]
$Cu(RSH)(H_2O)]_n$ + Eosin Y (1D-polymer)	N/A	≥ 420	7880 μmol g^{-1} h^{-1}		[34]
[Fe-Fe]@ZrPF	[FeFe} based complex	≥ 420	3.5 μmol h^{-1} in 120 min		[35]
UiO-66 Fe-Fe + $Ru(bpy)_3$	Fe-Fe	Blue LED 470 nm	* 280 μmol h^{-1} g^{-1}		[36]
POM@UiO-67	POM	≥ 400	699 μmol h^{-1} g^{-1} wrt POM		[37]
MIL-125-NH_2 (Ti)	Co(III)-oxime	≥ 408	*~637 μmol h^{-1} g^{-1}	**AQY:** 0.5 %	[1]
MIL-125-NH_2 (Ti)	Nickel (II) Species	≤ 360	*6693 μmol h^{-1} g^{-1}		[38]
Cu-I-bpy		UV-light Irradiation	7090 μmol h^{-1} g^{-1}		[39]
$\{[Cu^{I}Cu^{II}_2(DCTP)_2]NO_3 \cdot 1.5DMF\}_n$	H_2PtCl_6	320-780 nm	*32 μmol h^{-1} g^{-1}		[40]

** = calculated μmol h^{-1} g^{-1}*

Unless otherwise stated, H_2 rate in respect of MOF

S19. References

1. M. A. Nasalevich, R. Becker, E. V. Ramos-Fernandez, S. Castellanos, S. L. Veber, M. V. Fedin, F. Kapteijn, J. N. Reek, J. Van Der Vlugt and J. Gascon, *Energy Environ. Sci.*, 2015, **8**, 364-375.
2. D. P. Kumar, J. Choi, S. Hong, D. A. Reddy, S. Lee and T. K. Kim, *ACS Sustainable Chemistry & Engineering*, 2016, **4**, 7158-7166.
3. M. Dan-Hardi, C. Serre, T. Frot, L. Rozes, G. Maurin, C. Sanchez and G. Férey, *J. Am. Chem. Soc.*, 2009, **131**, 10857-10859.
4. C. Hatchard and C. A. Parker, *Proc. R. Soc. London, Ser. A*, 1956, **235**, 518-536.
5. H. Kuhn, S. Braslavsky and R. Schmidt, *Pure Appl. Chem.*, 2004, **76**, 2105-2146.
6. J. Hutter, M. Iannuzzi, F. Schiffmann and J. VandeVondele, *WIREs Comput. Mol. Sci.*. 2014, **4**, 15-25.
7. J. P. Perdew, K. Burke and M. Ernzerhof, *Phys. Rev. Lett.*, 1996, **77**, 3865.
8. S. Goedecker, M. Teter and J. Hutter, *Phys. Rev. B: Condens. Matter*, 1996, **54**, 1703.
9. J. VandeVondele and J. Hutter, *J. Chem. Phys.*, 2007, **127**, 114105.
10. C. H. Hendon, D. Tiana, M. Fontecave, C. Sanchez, L. D'arras, C. Sassoye, L. Rozes, C. Mellot-Draznieks and A. Walsh, *J. Am. Chem. Soc.*, 2013, **135**, 10942-10945.
11. M. Sharon, G. Tamizhmani, C. Levy-Clement and J. Rioux, *Solar Cells*, 1989, **26**, 303-312.
12. Y. Xu and M. A. A. Schoonen, *Am. Mineral.*, 2000, **85**, 543-556.
13. P. A. Osorio-Vargas, C. Pulgarin, A. Sienkiewicz, L. R. Pizzio, M. N. Blanco, R. A. Torres-Palma, C. Petrier and J. A. Rengifo-Herrera, *Ultrason. Sonochem.*, 2012, **19**, 383-386.
14. Z. K. Zheng, B. B. Huang, X. D. Meng, J. P. Wang, S. Y. Wang, Z. Z. Lou, Z. Y. Wang, X. Y. Qin, X. Y. Zhang and Y. Dai, *Chem. Commun.*, 2013, **49**, 868-870.
15. J. A. Mason, L. E. Darago, W. W. Lukens and J. R. Long, *Inorg. Chem.*, 2015, **54**, 10096-10104.
16. M. A. Nasalevich, C. H. Hendon, J. G. Santaclara, K. Svane, B. van der Linden, S. L. Veber, M. V. Fedin, A. J. Houtepen, M. A. van der Veen, A. Walsh and J. Gascon, *Nature Sci. Rep.*, 2016, **6**.
17. A. Y. Kang, P. M. Lenahan and J. F. Conley, *Appl. Phys. Lett.*, 2003, **83**, 3407-3409.
18. X. L. Zhang and K. J. Klabunde, *Inorg. Chem.*, 1992, **31**, 1706-1709.
19. K. Matsubara, Y. Fukahori, T. Inatomi, S. Tazaki, Y. Yamada, Y. Koga, S. Kanegawa and T. Nakamura, *Organometallics*, 2016, **35**, 3281-3287.
20. Y. Horiuchi, T. Toyao, M. Saito, K. Mochizuki, M. Iwata, H. Higashimura, M. Anpo and M. Matsuoka, *J. Phys. Chem. C*, 2012, **116**, 20848-20853.
21. D. Sun, W. Liu, M. Qiu, Y. Zhang and Z. Li, *Chem. Commun.*, 2015, **51**, 2056-2059.
22. T. Toyao, M. Saito, S. Dohshi, K. Mochizuki, M. Iwata, H. Higashimura, Y. Horiuchi and M. Matsuoka, *Chem. Commun.*, 2014, **50**, 6779-6781.
23. T. Toyao, M. Saito, Y. Horiuchi, K. Mochizuki, M. Iwata, H. Higashimura and M. Matsuoka, *Catal. Sci. Technol.*, 2013, **3**, 2092-2097.
24. A. Fateeva, P. A. Chater, C. P. Ireland, A. A. Tahir, Y. Z. Khimyak, P. V. Wiper, J. R. Darwent and M. J. Rosseinsky, *Angewandte Chemie*, 2012, **124**, 7558-7562.
25. X. Sun, Q. Yu, F. Zhang, J. Wei and P. Yang, *Catalysis Science & Technology*, 2016, **6**, 3840-3844.
26. L. Shen, M. Luo, L. Huang, P. Feng and L. Wu, *Inorg. Chem.*, 2015, **54**, 1191-1193.
27. D. Wang, Y. Song, J. Cai, L. Wu and Z. Li, *New J. Chem.*, 2016, **40**, 9170-9175.
28. T. Zhou, Y. Du, A. Borgna, J. Hong, Y. Wang, J. Han, W. Zhang and R. Xu, *Energy & Environmental Science*, 2013, **6**, 3229-3234.
29. J.-Q. Shen, Y. Zhang, Z.-M. Zhang, Y.-G. Li, Y.-Q. Gao and E.-B. Wang, *Chem. Commun.*, 2014, **50**, 6017-6019.
30. C. Wang, K. E. DeKrafft and W. Lin, *J. Am. Chem. Soc.*, 2012, **134**, 7211-7214.
31. C. Gomes Silva, I. Luz, F. X. Llabrés i Xamena, A. Corma and H. García, *Chem. Eur. J.*, 2010, **16**, 11133-11138.
32. J. He, J. Wang, Y. Chen, J. Zhang, D. Duan, Y. Wang and Z. Yan, *Chem. Commun.*, 2014, **50**, 7063-7066.
33. Y.-P. Yuan, L.-S. Yin, S.-W. Cao, G.-S. Xu, C.-H. Li and C. Xue, *Applied Catalysis B: Environmental*, 2015, **168–169**, 572-576.
34. X. Y. Dong, M. Zhang, R. B. Pei, Q. Wang, D. H. Wei, S. Q. Zang, Y. T. Fan and T. C. Mak, *Angew. Chem. Int. Ed.*, 2016, **55**, 2073-2077.
35. K. Sasan, Q. Lin, C. Mao and P. Feng, *Chem. Commun.*, 2014, **50**, 10390-10393.
36. S. Pullen, H. Fei, A. Orthaber, S. M. Cohen and S. Ott, *J. Am. Chem. Soc.*, 2013, **135**, 16997-17003.
37. Z.-M. Zhang, T. Zhang, C. Wang, Z. Lin, L.-S. Long and W. Lin, *J. Am. Chem. Soc.*, 2015, **137**, 3197-3200.
38. K. Meyer, S. Bashir, J. Llorca, H. Idriss, M. Ranocchiari and J. A. van Bokhoven, *Chemistry-A European Journal*, 2016, **22**, 13894-13899.
39. D. Shi, R. Zheng, M.-J. Sun, X. Cao, C.-X. Sun, C.-J. Cui, C.-S. Liu, J. Zhao and M. Du, *Angew. Chem. Int. Ed.*, 2017, **56**, 14637-14641.
40. Z.-L. Wu, C.-H. Wang, B. Zhao, J. Dong, F. Lu, W.-H. Wang, W.-C. Wang, G.-J. Wu, J.-Z. Cui and P. Cheng, *Angew. Chem. Int. Ed.*, 2016, **55**, 4938-4942.